RSC Advances

This article can be cited before page numbers have been issued, to do this please use: S. SENTHILVELAN, V. L. CHANDRABOSS, J. KAMALAKKANNAN and S. PRABHA, *RSC Adv.*, 2015, DOI:

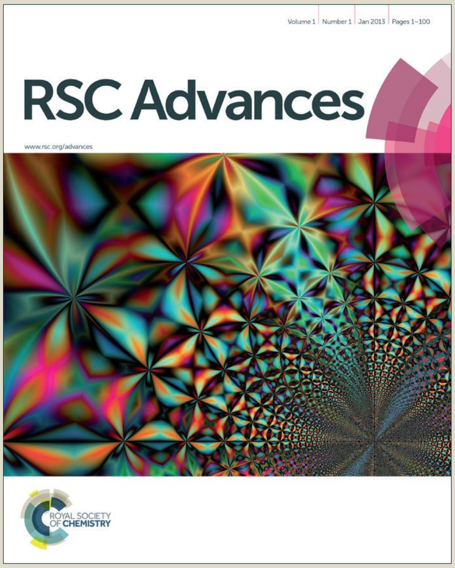

View Article Online
DOI: 10.1039/C4RA14463E

GRAPHICAL ABSTRACT

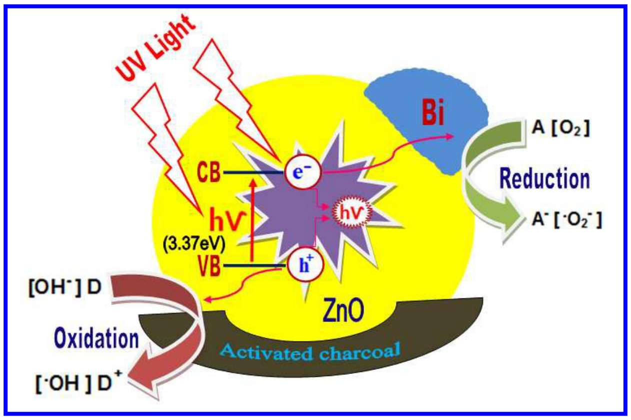

The hetero-junctions that are formed between the AC-supported Bi and ZnO, Bi provide an internal electric field that facilitates separation of the electron-hole pairs and induces faster carrier migration. Thus they often enhanced photocatalytic activity.

View Article Online
DOI: 10.1039/C4RA14463E

An Efficient Removal of Methyl Violet from Aqueous Solution by AC-Bi/ZnO Nanocomposite Material

V.L. Chandraboss, J. Kamalakkannan, S. Prabha and S. Senthilvelan*

Department of Chemistry, Annamalai University, Annamalainagar 608 002, Tamilnadu, India.

*Corresponding Author: dr_senthilvel@yahoo.co.in

ABSTRACT

Activated charcoal (AC) supported bismuth (Bi)-doped zinc oxide (ZnO) nanocomposite material was synthesized by precipitation method. The obtained material was characterized by high resolution-scanning electron microscopy (HR-SEM) with energy dispersive X-ray analysis (EDX), X-ray diffraction (XRD), Fourier transform-Raman spectroscopy (FT-RAMAN), photoluminescence spectra (PL), UV-Visible diffuse reflectance spectra (UV-Vis-DRS), X-ray photoelectron spectroscopy (XPS) and Brunauer–Emmett–Teller (BET) analysis. BET surface area, pore radius and pore volume of the materials were calculated by applying the BET equation to the sorption isotherms. The cyclic voltammetry (CV) analysis suggested that the electrochemical redox reaction. The production of hydroxyl radicals ($^{\bullet}$OH) on the surface of UV-irradiated photocatalysts was detected by photoluminescence technique using coumarin as a probe molecule. The photocatalytic activity of the AC-Bi/ZnO material is demonstrated through photodegradation of methyl violet (MV) under UV-light irradiation. AC-Bi/ZnO has increased absorption in the UV region; it shows excellent UV-light driven photocatalytic performance. The photocatalyst of AC-Bi/ZnO reveals enhanced photocatalytic activities as compared to the ZnO and Bi/ZnO for the degradation of harmful MV dye. The enhanced photocatalytic activity of AC-Bi/ZnO is attributed to the low recombination rates of photoinduced electron hole pairs, caused by transfer of electrons and holes between ZnO and AC supported Bi^{3+} ion. The mechanism of photocatalytic effect of the AC-Bi/ZnO

View Article Online
DOI: 10.1039/C4RA14463E

nanocomposite material has been discussed. AC-Bi/ZnO proposed that use of water purification technique is promising.

Keywords: Photocatalysis, Activated charcoal, Zinc oxide, Nanocomposite, UV-light.

1. INTRODUCTION

Nowadays, water sources are facing serious threat from hazardous pollutants due to various activities. These hazardous compounds include heavy metals, anions, organic compounds and dyes. These contaminants could threaten public health and the atmosphere when they exceed the tolerance limits in water.[1–4] Every day a large amount of unconsumed dye produced by textile and printing industries are discharged in to the environment. The presence of dyes and pigments in water causes considerable damage to the marine environment.[5–7] Basic dyes have high intensity of colour and are extremely toxic even in a very low concentration.[8–10] Methyl violet (MV) may cause severe skin and eye irritation. Inhalation of MV may also cause irritation to respiratory tract, whereas ingestion causes irritation to gastrointestinal tract.[11] Hence, the dye removal is of enormous value.

Metal oxide is the most excellent choice for heterogeneous photocatalysis to remove various pollutants, dyes and phenolic compounds.[12-15] Among the metal oxides ZnO is alternative for TiO_2 due to the similar band gap energy (3.37 eV), similar phototocatalytic mechanism and capacity.[16-18] ZnO is a semiconductor with high photosensitivity, non-toxic nature, low cost, and environmentally friendly features for photocatalytic applications.[19] ZnO has a competitive photocatalytic activity greater in some cases than TiO_2, for example, in the decolourization of Reactive Blue19, textile dyes and azo dyes in aqueous suspension.[20-22] Furthermore, semiconductor thin films have been found to photodegrade the dyes and insecticides.[23,24] ZnO nanoparticles can be prepared via various methods hydrothermal, electro deposition (ED), chemical vapor deposition (CVD), electrochemical, solution combustion, sol–gel and

View Article Online
DOI: 10.1039/C4RA14463E

precipitation method.[25-31] Among all methods, precipitation technique provides suitable control of nucleation, ageing and growth of particles in solution. The direct precipitation is also one of the simple and cost effective methods for bulk production of materials.[32] As known, both the size and the morphology have an influence on the properties of photocatalysts.[33]

In this method, particle growth owes to interact between different aqueous solutions and therefore very small particles are formed. Small size particles with lower solubility product dissolve and re-precipitate on the surface of larger particles in solution; therefore agglomeration takes place in solution as the particles clog together to decrease surface energy.[34] Doping is one of the most widely used strategies to increase the photocatalytic activity of semiconductors.[35] Many dopants such as transition metals (Mn, Cu and Co) and rare earth elements (La, Ce and Er) could enhance the photocatalytic properties of ZnO.[36-39] The effect of Bismuth-doped ZnO nanocomposite material for the photocatalytic degradation of Congo Red was discussed very recently.[31] Doping of Bi into ZnO is expected to shift the absorption edge of ZnO and influence the separation rate of photoinduced charge carriers of ZnO because of the different structure of the electronic shell and size of Bi and Zn.[40] Bismuth is a kind of p-block metal with a d10 configuration, and the hybridized valence band by O 2p and Bi 6s can narrow the band gap, as well as favor the mobility of photo-generated holes in the valance band.[41,42] It is worth noting that about the studies of bismuth-based photocatalysts focus on degradation of organic pollutants.[43,40]

The Photocatalytic oxidation is an economical process owing to the fact that it involves only a photocatalyst and light source.[44] An alternative approach for decolourization methods is the addition of charcoal due to its valuable features in the chemical, physical or biological process.[45-47] The function of charcoal is versatile: (i) it acts as a dye adsorbent, not only in straight forward adsorption processes but also in charcoal enhanced coagulation and membrane filtration processes; (ii) it catalyses $^{\bullet}OH$ production

View Article Online
DOI: 10.1039/C4RA14463E

in advanced oxidation processes; (iii) it generates strong oxidizing agents (mostly, hydroxyl ($^{\bullet}$OH) radicals) in electrochemical dye oxidation; (iv) it catalyses anaerobic (azo) dye reduction and supports biofilm growth in microbial dye removal.[48] Although charcoal is having higher adsorption property, it usually does not degrade the dye. But charcoal loaded on semiconductor oxide enhances the degradation efficiency of semiconductor oxide by its synergetic effect and effective degrades the dye. The increase in photocatalytic activity of semiconductor oxide by the addition of charcoal has been well established.[49,50]

In this work, we report the synthesis, characterization and photocatalytic activity of AC-supported Bi-doped ZnO nanocomposite material. AC-Bi/ZnO material was synthesized by a simple and cost effective precipitation method. The obtained material was characterized by HR-SEM with EDX, XRD, FT-RAMAN, PL, DRS, XPS, BET and CV analysis. In application part, we have studied their photocatalytic activity towards MV in aqueous solution under UV-light irradiation. Here, we highlight and evaluate recent progress in the development of photocatalytic activity of AC-Bi/ZnO nanocomposite material. The enhanced photocatalytic activity of AC-Bi/ZnO is caused by the reduction of the recombination of electron-hole pairs, decrease the band gap energy, increasing surface area, degree of aggregation, increase of $^{\bullet}$OH formation, improve the electron transfer and increase of absorption of light intensity are desired elaborately. The AC-Bi/ZnO reveals enhanced photocatalytic activities as compared to ZnO and Bi/ZnO for the degradation and decolourization of MV under UV-light irradiation for 0-60 minutes.

2. EXPERIMENTAL SECTION

2.1. Materials

Zinc acetate dihydrate ($Zn(CH_3COO)_2 \cdot 2H_2O$), bismuth nitrate pentahydrate ($Bi(NO_3)_3 \cdot 5H_2O$), activated charcoal, oxalic acid ($C_2H_6O_6$), anhydrous ethanol (C_2H_5OH), coumarin (1 mM of 4-hydroxy

View Article Online
DOI: 10.1039/C4RA14463E

coumarin) and Methyl Violet ($C_{25}H_{30}ClN_3$) were the guaranteed reagents of Sigma Aldrich and used as such. The aqueous solutions were prepared by using double distilled water.

2.2. Synthesis of AC supported Bi-doped ZnO nanocomposite material

AC supported Bi-doped ZnO nanocomposite material was synthesized by precipitation method (Scheme 1). 0.24 g of $Bi(NO_3)_3.5H_2O$ (0.1 M) and 0.003 g of activated charcoal (0.05 M) together with a 0.4 M of oxalic acid were dissolved in 20 mL of anhydrous ethanol. The resulting solution was added dropwise into 20 mL solution of 2.7 g of $Zn(CH_3COO)_2 \cdot 2H_2O$ (0.8 M) in anhydrous ethanol at room temperature under vigorous stirring until precipitate formed. The obtained precipitate was washed with water and ethanol. Then the precipitate was collected and dried in oven at 100 ^{o}C for 12 h in air. The resulting powder was finally calcined at 600 ^{o}C for 3 h in a muffle furnace to get AC-Bi/ZnO. It is found that this catalyst contained 8.5 wt % of AC, 21.5 wt % of Bi and 70 wt % of ZnO. The bare ZnO and Bi-doped ZnO nanocomposites are also synthesized by the same precipitation method.

2.3. Analysis of hydroxyl radical ($^{\bullet}$OH)

The formation of hydroxyl radicals ($^{\bullet}$OH) are similar to the photocatalytic activity experiment.[51] Photoluminescence (PL) technique with coumarin (1 mM) as a probe molecule was used to investigate the formation of hydroxyl radical on the surface of AC-Bi/ZnO illuminated by UV irradiation for 0 to 60 min.

2.4. Adsorption and oxidation kinetics on the surface of AC-Bi/ZnO material

Activated charcoal (AC) is excellent adsorbents of countless pollutants. Their industrial applications involve the adsorptive removal of odour, colour, taste and other unwanted organics and inorganics from waste water and drinking water.[48] The organic substrates from dye effluents diluted in aqueous medium are considered to be first adsorbed on the surface of the AC (Fig. 1), where they migrate to the Bi/ZnO particles and they are oxidized in the vicinity of Bi/ZnO by radical species such as hydroxyl

DOI: 10.1039/C4RA14463E

radicals ($^{\bullet}OH$) and superoxide radical anions ($O_2^{\bullet-}$) which are formed by the reaction with photogenerated holes (h^+) and electrons (e^-) respectively. Hence, a good understanding of the physicochemical properties of the support materials is very important to achieve efficient photodegradation.

2.5. Photocatalytic activity

The photocatalytic activity of the photocatalyst was evaluated by the photodegradation of MV. The light source was a UV lamp. The reaction was maintained at ambient temperature (303 K). In a typical experiment, aqueous suspensions of dye (40 mL, 2×10^{-4} M) and 0.08 g of the photocatalyst powder were placed in reaction tubes. Prior to irradiation, the suspension was magnetically stirred in the dark to ensure the establishment of an adsorption/desorption equilibrium. The suspension was kept under constant air-equilibrated condition. At the intervals of given irradiation time. The suspension was measured spectrophotometrically (573 nm) by diluting it four times to keep the absorptions within the Beer–Lambert law limit.

2.6. Characterization methods

High-resolution scanning electron microscopy and elementary dispersive X-ray analysis experiments were carried out on a FEI Quanta FEG 200 instrument with EDX analyzer facility at 25 °C. The sample was prepared by placing a small quantity of prepared nanocomposites on a carbon coated copper grid and allowing the solvent to evaporate. X-ray diffraction spectra was recorded on the X'PERT PRO model X-ray diffractometer from Pan Analytical instruments operated at a voltage of 40 kV and a current of 30 mA with Cu Kα radiation. Fourier transform-Raman spectra were recorded with an integral microscope Raman system RFS27 spectrometer equipped with 1024 X 256 pixels liquefied nitrogen-cooled germanium detector. The 1064 nm line of the Nd:YAG laser (red laser) was used to excite. To avoid intensive heating of the sample, the laser power at the sample was not higher than 15 mW. Each

View Article Online
DOI: 10.1039/C4RA14463E

spectrum was recorded with an acquisition time of 18 sec. Photoluminescence spectra at room temperature were recorded using a Perkin-Elmer LS 55 fluorescence spectrometer. Nanoparticles were dispersed in chloroform and excited using light of wavelength 300 nm. The UV-Visible diffuse reflectance spectra of nanomaterials were recorded with a UV-3600 SHIMADZU (Japan) spectrometer in the range of 800–200 nm. To determine the textural properties of the synthesized materials, N_2 adsorption–desorption measurements were carried out at 77 K using a Micromeritics ASAP 2020 V3.00 H instrument. X-ray photoelectron spectroscopy analysis were performed on a monochromatic Al Kα source instrument (Omicron Nanotechnology, GMBH, Germany) operating at 14 kV and 20 mA for an X-ray power of 280 W. Spectra were collected with a photoelectron take-off angle of 90^o from the sample surface plane with energy steps of 0.10 eV and pass energy of 20 eV. The spectra were referenced to the binding energy of C (1s) (285 eV). The BET method was utilized to calculate the specific surface area of the materials. By using the Barrett–Joyner–Halenda (BJH) model, the pore size distribution was derived from the desorption branches of the isotherms at a relative pressure (P/Po) of 0.98. Cyclic voltammograms (CVs) were performed by using a CHI 604C electrochemical analyzer (CHI Instruments Inc., Austin, TX). A conventional three-electrode cell was used, including an Ag/AgCl (saturated KCl) electrode as the reference electrode, a Pt wire served as a counter electrode, and glassy carbon electrode (GCE) coated with synthesized AC-Bi/ZnO as a working electrode. UV-vis (ultraviolet and visible light) absorbance spectra were measured over a range of 800-200 nm with a Shimadzu UV-1650PC recording spectrometer using a quartz cell with 10 mm of optical path length.

View Article Online
DOI: 10.1039/C4RA14463E

3. RESULTS AND DISCUSSION

3.1. Surface morphology and elemental analysis

HR-SEM images of the Bi/ZnO and AC-Bi/ZnO nanocomposites are shown in Figs. 2a and 2b respectively. The HR-SEM images revealed that individual particles were composed by a collection of elongated particles of various size and shapes. HR-SEM images of the Bi/ZnO shows the average particle size of 80 nm and AC-Bi/ZnO shows the average particle size of 30 nm. The above observation particles size of the Bi/ZnO was greater than that of AC-Bi/ZnO suggesting that in absence of AC. The Bi/ZnO aggregates more easily during the calcination process. AC acted as a barrier which controlled the growth of Bi/ZnO particles and prevents their aggregation. Aggregation of particles would inevitably reduce their total surface area exposed to the outer environment, leading to a lowered photocatalytic activity as observed in many reaction systems.[18] Moreover, the decrease in particle size can be correlated with the observed increase of the surface area. This can be further discussed in BET surface area analysis. The surface properties, undoubtedly, have a great influence on the photocatalytic activity.[52] AC-Bi/ZnO is caused by larger surface area, increased oxygen vacancy, increases the absorption of light intensity and enhances the photocatalytic activity. EDX analysis confirms Zn, Bi and O are present in Bi/ZnO (Fig. 2c), Whereas Zn, Bi, C and O are present in AC-Bi/ZnO composite material (Fig. 2d). EDX analysis clearly displays intense peaks between 2.0 and 2.5 keV corresponding to bismuth L1 (2.3 keV), which is similar to the major constituents of the Bi/ZnO and AC-Bi/ZnO.

3.2. XRD analysis

The obtained XRD of the ZnO, Bi/ZnO and AC-Bi/ZnO nanocomposites are shown in Figs. 3a, 3b and 3c respectively. The peaks at 31.7°, 34.3°, 36.2°, 47.4°, 56.5°, 62.8°, and 67.8° are from the diffractions for ZnO (100), (002), (101), (102), (110), (103) and (112) crystal planes (JCPDS No.

View Article Online
DOI: 10.1039/C4RA14463E

36-1451). The relatively high intensity of the (101, 002 and 100) peaks are indicative of anisotropic growth and implies a preferred orientation of the crystallites.[53,54] The peaks at 22.5°, 24.8°, 30.1°, 33.6°, 36.2°, 40.4°, 47.2°, and 56.1° are the diffractions of the Bi (003), (101), ZnO (100), (002), (101), Bi (110) and ZnO (102), (110) crystal planes. It confirms the Bi^{3+} was present in ZnO lattice[40] (JCPDS No. 36-1451, 44-1246 and 79-0206).

AC-Bi/ZnO, peaks at 26.5°, 27.1°, 31.9°, 34.6°, 36.1°, 44.8°, 50.2°, 56.1° and 60.2° are the diffractions of the C (300), Bi (012), ZnO (100), (002), (101), Bi (015), C (511), ZnO (110), C (161) crystal planes. It shows Bi and C are present in ZnO material (JCPDS No. 36-1451, 44-1246 and 50-0927). As shown in Fig. 3, all strong peaks can be indexed as the pure hexagonal phase of wurtzite-type ZnO, which agrees well with the reported data (JCPDS No. 36-1451 and 79-0206). This results indicate that AC-supported Bi-doped ZnO have a hexagonal phase of wurtzite structure. The sharp peaks of ZnO indicate the high degree of crystallinity (Fig. 3a). An addition of Bi and AC in the AC-Bi/ZnO decreases the peak intensity of (101), (001) and (100) diffraction planes, which indicate AC act as barrier and Bi^{3+} in the lattice of ZnO. Fig. 3b and 3c shows the diffraction peaks (002) are slightly left-shifted, which is mainly due to the larger radius of Bi^{3+} versus that of Zn^{2+}. This observation suggests that a portion of Bi^{3+} ions was incorporated into the ZnO lattice[55] by replacing Zn^{2+} with Bi^{3+}.

The average crystalline size (*L*) of the ZnO, Bi/ZnO and AC-Bi/ZnO particles are calculated by the Debye-Scherrer formula,[56] $L=0.89\lambda/\beta\mathrm{COS}\theta$ where *L* is the crystalline size (in nm), λ is the wavelength (in nm), β is the full width at half maximum intensity (FWHM-in radian), and θ is the Bragg diffraction angle (^{o}). The average crystalline size of ZnO and Bi/ZnO composite was figured out to be about 92.5 and 78.5 nm. The average crystalline sizes of AC-Bi/ZnO composite are almost 29.5 nm.

View Article Online
DOI: 10.1039/C4RA14463E

3.3. FT-RAMAN analysis

The Raman spectra of the ZnO, Bi/ZnO and AC-Bi/ZnO are shown in Fig. 4. The characteristic peaks at 212, 380, 438, 569, 1150 cm^{-1}, which correspond to the 2TA; 2E$_2$(low), A$_1$(TO), E$_2$(high), A$_1$(LO) and 2A$_1$(LO), 2E$_1$(LO); 2LO fundamental phonon modes of ZnO, respectively. The Raman peak at 438 cm^{-1} is attributed to the ZnO nonpolar optical phonons of high-E2 mode,[57] which is one of the characteristic peaks of wurtzite ZnO (Fig. 4a).

Bi/ZnO shown peaks at 229, 549, 592, 912, 1080, 1472 cm^{-1} (Fig. 4b). The characteristic peaks at 229, 549, 592 cm^{-1} which correspond to the shifted peaks of 2TA; 2E$_2$(low), A$_1$(LO) and E$_1$(LO) respectively. The peak at 229 cm^{-1} attributed to the 2TA; 2E$_2$(low) mode, which is one of the characteristic peak of Bi-O bonds. The band at 549 cm^{-1} corresponds to A$_1$ symmetry with LO modes. The A$_1$(LO) become a sharp peak and shifted about 20 cm^{-1} towards lower energy. It is generally accepted that the A$_1$(LO) peak caused by polar branches appeared at about 549 cm^{-1} respectively. From the above observation Bi was present in ZnO nanomaterial is confirmed. AC-supported Bi/ZnO shows peaks at 232, 323, 441, 1580 cm^{-1} (Fig. 4c). The shifted peaks at 232 and 323 cm^{-1} attributed to the 2TA; 2E$_2$(low) and E$_2$(high)-E$_2$(low) mode, which is one of the characteristic peak of Bi-O bonds. The shifted peak at 441 cm^{-1} is attributed to the high-E$_2$ mode, which is one of the characteristic peaks of wurtzite ZnO. Above 400 cm^{-1} the intensity of the peaks are increased, several small peaks also observed. The high intensity of the 1580 cm^{-1} assigned to G-band, which correspond to carbon present in the Bi/ZnO composite.

3.4. PL analysis

Photoluminescence spectra of ZnO, Bi/ZnO and AC-Bi/ZnO are shown in Figs. 5a, 5b and 5c respectively. As the photoluminescence occurs due to electron–hole recombination, its intensity is directly

View Article Online
DOI: 10.1039/C4RA14463E

proportional to the rate of electron−hole recombination.**[58]** ZnO showed four emissions at 400, 436, 480 and 530 nm. Bi/ZnO showed four emissions at 401, 438, 482 and 531 nm. AC-Bi/ZnO also showed four emissions at 401, 438, 487 and 531 nm. AC-supported Bi-doping of ZnO slightly shifts the emission of ZnO. AC-Bi/ZnO shows a near UV emission band at 401 nm and a blue–green band at 487 nm. However, the PL intensity of 401 nm is lower than that of the synthesized ZnO. This near UV emission corresponds to the exciting recombination related near-band edge emission of the ZnO nanomaterial.**[59-62]** The blue–green emission is due to surface defects in the ZnO.**[62]** A reduction of PL intensity at 401 nm by AC-Bi/ZnO when compared to synthesized ZnO and Bi/ZnO indicates the suppression of the recombination of the photogenerated electron−hole pair by AC-Bi/ZnO. This leads to a higher photocatalytic activity of AC-Bi/ZnO nanocomposite material.

3.5. UV–Vis- DRS analysis

The UV-Vis –DRS spectra of ZnO, Bi/ZnO and AC-Bi/ZnO are shown in Fig. 6. The direct band gap of synthesized materials has been determined from the Tauc plots. Plots of $[F(R)h\nu]^2$ versus the photon energy (h_V) provide the direct band gap of the synthesized ZnO, Bi/ZnO and AC-Bi/ZnO as 3.19, 3.15 and 3.12 eV, respectively. UV–Vis-DRS results demonstrated that the decrease in the direct band gap of AC-Bi/ZnO compared to ZnO and Bi/ZnO. These results reveal AC-Bi/ZnO will be used as an effective photocatalyst. In addition, the UV-vis spectrum in the diffuse reflectance mode (R) was transformed to the Kubelka–Munk (KM) function, F(R) to separate the extent of light absorption from scattering.**[63]** F(R) values have been calculated from the reflectance (R) by application of the Kubelka–Munk algorithm: $[F(R) = (1 - R)^2/2R]$.**[64,65]** KM plot (Fig. 6d) shows that AC-Bi/ZnO is strong absorption in the UV region of 200–400 nm indicating more photocatalytic activity in UV region. This reveals that AC-Bi/ZnO can be

View Article Online
DOI: 10.1039/C4RA14463E

used as an UV light active photocatalytic material. Strong UV light absorption may lead to improved generation of electron-hole pairs, which enhances the photocatalytic activity of AC-Bi/ZnO.

3.6. XPS analysis

The composition and chemical states of the elements in AC-Bi/ZnO were examined by X-ray photoelectron spectroscopy. The typical X-ray photoelectron survey spectrum of the AC-Bi/ZnO indicates that the material consists of Zn, Bi, O and C (Fig. 7). The O 1s profile is asymmetric and can be fitted to two symmetrical peaks α and β located at 530.5 and 533.5 eV, indicating two different kinds of O species in the sample. These peaks should be associated with lattice oxygen of ZnO and chemisorbed oxygen caused by the surface hydroxyl (OH), respectively.[66] The C 1s peak is attributed to the activated charcoal present in the synthesized material.[67] XPS spectra of Zn 2p, and the peak positions of Zn 2p 1/2 and Zn 2p 3/2 are located at 1045.5 eV and 1019.9 eV. Comparing the peak positions to those in the Handbook of X-ray Photoelectron Spectroscopy,[68] we can conclude that Zn is in the state of Zn^{2+}. The peaks of Bi 4f 5/2 and Bi 4f 7/2 at 158.9 and 164.2 eV reveal that bismuth is in the state of Bi^{3+}.[69,70]

3.7. BET surface area analysis

The corresponding N_2 adsorption–desorption isotherms and BJH desorption pore distribution of all the investigated catalysts are shown in Fig. 8. The surface area of ZnO, Bi/ZnO and AC-Bi/ZnO was determined using the nitrogen gas adsorption method. N_2 adsorption–desorption isotherms of the catalysts exhibited a hysteresis loop, typical of a type II pattern representing the predominant nonporous structure according to the international union of pure and applied chemistry (IUPAC) classification.[71] A sharp increase in the adsorption volume of N_2 was observed and located in the P/Po at 0.98. This sharp increase can be attributed to the capillary condensation, indicating the good homogeneity of the sample and a macro pore size, since the P/P_0 position of the inflection point is related to the pore size.[72] The pore size

View Article Online
DOI: 10.1039/C4RA14463E

distribution of ZnO, Bi/ZnO and AC-Bi/ZnO are given in inset Fig. 7a, 7b and 7c respectively. The BET surface and total pore volume of the catalysts was given in Table 1. BET surface area of AC-Bi/ZnO (19.4 m²/g^{-1}) is higher than Bi/ZnO (15.3 m²/g^{-1}) and bare ZnO (8.3 m²/g^{-1}). It is clear that Bi^{3+} doped is effective for changing the morphology of ZnO, the big particle size leads to the BET surface area decrease, this result agrees well with the result of BET surface area. Higher surface area of the AC-Bi/ZnO enhances the photocatalytic activity.

3.8. Electrochemical enhancement study

Photocatalysis is a surface phenomenon as the photogenerated charge carriers diffuse to the surface to initiate redox reactions.[73] The modified electrode was constructed by ZnO and AC-Bi/ZnO via mechanical attachment. Fig. 9. shows the effects of using unmodified/modified GCE on the electrochemical oxidation/reduction potential of potassium chloride (KCl) based on data from cyclic voltammetry. When the GCE was not modified with any photocatalyst, there is hardly any enhancement or decrement in the cycles. ZnO modified GCE was observed that the electrochemical oxidation of KCl is an irreversible process due to the peak (anodic current and the (Epa) peak potential of 0.931 V). But, AC-Bi/ZnO modified absence of a well-defined reduction GCE was observed that the electrochemical redox reaction of KCl is a reversible process (enhanced anodic and cathodic current and the (Epa) peak potential of 0.547 V and 0.245 V). These results indicated that AC-Bi/ZnO modified GCE had larger adsorption/desorption and higher electrochemical response than that of ZnO. Several literatures have indicated that the GCEs modified metal ion and carbon materials were found to perform better in comparison to bare GCE.[63,74,75] This suggests that the presence of AC and Bi in the ZnO could increases current and improve the relative electron transfer.

View Article Online
DOI: 10.1039/C4RA14463E

3.9. Hydroxyl radical analysis

The photocatalytic activity of as-synthesized materials was further confirmed by the detection of $^{\bullet}OH$. In order to confirm the existence of hydroxyl radicals, the formed hydroxyl radicals on the surface of AC-Bi/ZnO illuminated by UV light were detected by PL technique. The PL emission spectra excited at 330 nm in coumarin solution suspension with AC-Bi/ZnO were measured at different time intervals 0, 30 and 60 mins. Fig. 10a displays that a PL signals were observed at 391 to 522 nm. The main peak is respectively located at about 391, 398, 404, 417, 447 and 522 nm respectively. The occurrence of emission peaks observed in the UV-visible region is attributed to the electronic transition mediated by the defect levels such as oxygen vacancies in the band gap.[76,77] The maximum PL intensity was found for AC-Bi/ZnO at 60 min (Fig. 10b). This suggests that the fluorescence is caused by chemical reactions of coumarin with hydroxyl radicals formed in photocatalytic reactions.[51] Hence, hydroxyl radical is the reactive oxidation species in AC-Bi/ZnO sample and finally induces the degradation of MV. Moreover, AC-Bi/ZnO with maximal photocatalytic activity produced much more reactive hydroxyl radicals.[78] Increase of $^{\bullet}OH$ formation on AC-Bi/ZnO can be caused by the better separation of free carriers retarding the recombination reaction in the semiconductor through the capture of electrons by AC-Bi/ZnO and enhanced yield of reaction between photogenerated holes and adsorbed water molecules on the photocatalyst surface.

3.9.1. Photocatalytic performance of AC-Bi/ZnO nanocomposite material

Dye effluents from textile industries are becoming a severe environmental trouble because of their high chemical oxygen demand content, resistance to chemical, unacceptable colour, photochemical and biological degradation.[79] We have chosen photodegradation of MV as model dye with UV irradiation to evaluate the photocatalytic activity of the proposed photocatalyst. Fig. 11 shows the time course of

View Article Online
DOI: 10.1039/C4RA14463E

decrease in the absorbance of MV under UV light irradiation. The photodegradation process of MV, the UV–vis spectra and the colours of MV aqueous solution as a function of UV-light irradiation time in the presence of photocatalysts (ZnO, Bi/ZnO and AC-Bi/ZnO) are illustrated in Figs. 11a, 11b and 11c. It can be seen from UV–visible spectra changes, the strong adsorption peak of MV solution at 573 nm steadily decreased and degraded with increasing the light irradiation time, and the initial violet colour of the solution gradually turned to light-coloured. Comparative studies of photocatalytic activity of ZnO, Bi/ZnO and AC-Bi/ZnO photocatalysts for photodegradation as well as decolourization of MV was shown in Fig. 11d. AC-Bi/ZnO exhibited excellent photocatalytic activity for MV under UV-light irradiation when compared to that of ZnO and Bi/ZnO.

Fig. 12a shows the time course of percentage decolourization of MV under UV-light irradiation. After 60 min of irradiation time AC-Bi/ZnO can decolourize the MV in aqueous solution up to 94.5 % when compared to that of ZnO and Bi/ZnO (66.5% and 82.5%) respectively. Under dark conditions, initially there is a decrease in dye concentration with AC-Bi/ZnO and this is due to the adsorption of the dye on the catalyst. Under UV light irradiation, degradation of MV occurred with all the catalysts. However, AC-Bi/ZnO exhibited higher photocatalytic activity than ZnO and Bi/ZnO photocatalysts. Fig. 12b shows the time course of decrease in the concentration of MV under UV-light irradiation. Initially MV dye concentration was 2×10^{-4} M after photodegradation takes place with respect of time. The blank run (air passing) was 30 minutes 1.4×10^{-4} M than UV-irradiation takes at 0 to 60 minutes. After 60 minutes of irradiation time AC-Bi/ZnO can photodegradation of MV in aqueous solution up to 5.4×10^{-5} M when compared to that of ZnO and Bi/ZnO (7.4×10^{-5} M and 6.4×10^{-5} M) respectively. It can be seen that increase the irradiation time (0 to 60 minutes) with respect to decrease the dye concentration, therefore AC-Bi/ZnO shows higher photocataltyic activity. As shown in Fig. 12, no significant photodegradation of

View Article Online
DOI: 10.1039/C4RA14463E

MV was observed in the absence of AC and Bi, which indicated that the photosensitizing effect of MV could be ignored in this case. It was also found that AC-Bi/ZnO showed much higher photocatalytic efficiency than ZnO, and exhibited the best photocatalytic performance for MV photodegradation.

Fig. 13a, evaluated by measuring the time dependent degradation efficiency of MV in an aqueous catalyst suspension under UV light exposure. Because MV itself is a dye which is active to UV-light, its photocatalytic activity is in the order of the AC-Bi/ZnO > Bi/ZnO > ZnO. The photodegradation kinetics of MV on ZnO, Bi/ZnO and AC-Bi/ZnO were evaluated using the pseudo-first-order model:

$$\ln(C_{0/}C_t) = K_{app}t \qquad (1)$$

Where $K_{app}t$ is the rate constant [min], C_0 is the initial concentration of MV, and Ct is the concentration of MV at reaction time (t)[80] From the results (Fig. 13b), one can see that AC-Bi/ZnO showed the highest degradation rate constant, approximately 1.098 × 10^{-4} sec^{-1}, which was greater than that of ZnO (~0.822 × 10^{-4} sec-^{1}) and Bi/ZnO (~0.958 × 10^{-4} sec-^{1}).

AC-Bi/ZnO generally accepted that the photocatalytic activity is initiated by the photogeneration of electron–hole pairs. The $^{\bullet}OH$ radicals, produced by an electron and the holes, are the primary oxidative species in a photocatalytic degradation and decoloration reaction, and they attack azo group causing the decomposition of chromophores.[81-83] Photocatalytic process is influenced by various factors, in which specific surface area and the transport properties of photoinduced charge carriers are two key factors.[84] The AC-Bi/ZnO is quite active for photocatalytic MV degradation, because they have a larger BET surface area (19.4 m^2/g^{-1}) than the prepared ZnO (8.3 m^2/g^{-1}) and Bi/ZnO (15.3 m^2/g^{-1}) to facilitate a more efficient of the AC-Bi/ZnO with organic dye contaminants and thus resulting in enhanced photocatalytic activity. UV-Vis-DRS (Fig. 6d) shows AC-Bi/ZnO is strong absorption in the UV region of 200–400 nm, there is a slight increase in absorbance in visible region. Hence AC-Bi/ZnO can be used as an UV light

View Article Online
DOI: 10.1039/C4RA14463E

active semiconductor photocatalytic material. Therefore, an experiment was conducted to test its photocatalytic activity under solar light (sunny days between 11 am and 12 pm). Irradiation of MV solution (2×10^{-4} M) with a borosilicate glass tube of 50 mL capacity (40 mL of MV solution with 0.08g of catalyst) for 1 hour, under the same condition was discussed in UV-light. Under solar light produced 70% of decolourization (degradation at 7.0×10^{-5} M). 94.5% decolourization (degradation at 5.4×10^{-5} M) was obtained with UV light. AC-Bi/ZnO shows higher photocatalytic activity due to the reduced band gap energy, smaller particle size, electron hole recombination and enhanced surface area which are the determining factors of enhanced photocatalytic efficiency.

3.9.2. The mechanism of photocatalytic effect of AC-Bi/ZnO nanocomposite material

AC-supported Bi-doped ZnO nanocomposite material absorb UV light and an electron from its valence band (vb) get excited to the conduction band (cb) generating a positively charged hole in the valence band (h^+_{vb}) and negative charge in the conduction band (e^-_{cb}) according to the Eqn. (2).

The chemisorbed H_2O molecules interact with the valence band holes forming $^\bullet OH$ radicals (Eqn. (3)), which attack dye molecule successively to make degradation. Furthermore, the conduction band electrons e^-_{cb} interact with dissolved O_2; producing superoxide radical anion ($O_2^{\bullet-}$) as shown in Eqn. (4). On the other hand, h^+_{vb} could interact with donor ^-OH and $HO_2^\bullet$ forming $^\bullet OH$ radical attack the dye as in Eqn. (5)

$$\text{AC-Bi/ZnO} + hv \rightarrow h^+_{vb} + e^-_{cb} \tag{2}$$

$$(H_2O \rightarrow H^+ + OH^-) + h^+_{vb} \rightarrow H^+ + {}^\bullet OH \tag{3}$$

$$O_2 + e^-_{cb} \rightarrow (O_2^{\bullet-}) + (H^+ + OH^-) \rightarrow HO_2^\bullet + {}^-OH \tag{4}$$

$$HO_2^\bullet + {}^-OH + h^+_{vb} \rightarrow {}^\bullet OH \tag{5}$$

View Article Online
DOI: 10.1039/C4RA14463E

Thus the Photocatalytic cycle comprises three steps (i) Illumination induces a transition of electrons from the valance band (VB) to the conduction band (CB), leaving an equal number of vacant sites (holes), (ii) The excited electrons and holes on Bi ion migrate to ZnO surface, facilitating the charge separation and higher photocatalytic efficiency. This charge separation is also revealed by the reduction of PL intensity of the proposed catalyst when compared to ZnO. This process not only facilitates the charge separation, but also accumulates electrons and holes in Bi and ZnO respectively. If large proportion of electron hole pairs recombine, dissipating the input energy in the form of heat or emitted light. To prevent the recombination of electron-hole pairs, AC-supported Bismuth on the ZnO surface acts as a barrier (Fig. 14). Effective electron–hole pair separation at the heterojunction interfaces can significantly improve photocatalytic performance of composite materials.[73,85] The hetero-junctions that are formed between the AC-supported ZnO and Bi provide an internal electric field that facilitates separation of the electron-hole pairs and induces faster carrier migration. (iii) The $^{\bullet}$OH radical was commonly recognized as the main reactive species responsible for the degradation of organic dyes.[86,87] The photogenerated electrons could react with the oxygen molecule adsorbed on the surface of AC-Bi/ZnO to yield $O2^{\bullet-}$. On the other hand, photogenerated holes react with H_2O molecules to produce $^{\bullet}$OH. $O2^{\bullet-}$, $^{\bullet}$OH and photogenerated holes to degrade the reactive dyes absorbed on the surface of AC-Bi/ZnO. Thus they often enhanced photocatalytic activity.

4. CONCLUSION

AC-supported Bi-doped ZnO nanocomposite material was synthesized by a precipitation method, and characterized by HR-SEM with EDX, XRD, FT-RAMAN, PL, DRS, XPS, BET and CV analysis. Results confirmed the formation of AC-Bi/ZnO nanocomposite material. HR-SEM and XRD analysis of ZnO and Bi/ZnO showed the average particle size of 78.4 nm, But AC-Bi/ZnO showed the average

DOI: 10.1039/C4RA14463E

particle size of 29.5 nm. The decrease in particle size can be correlated with the observed increase of the surface area. XRD, EDX and XPS reveal the presence of Zn, O, Bi and C and their oxidation states in the AC-Bi/ZnO. In XRD spectra all strong peaks are indexed as the pure hexagonal phase of wurtzite structure. FT-Raman spectra reveals that optical phonons of high-E2 mode, which corresponds to the wurtzite ZnO structure. PL spectra confirm suppression of recombination of the photogenerated electron−hole pairs by AC-Bi/ZnO nanomaterial. UV-Vis-DRS demonstrated that the decrease in the direct band gap of AC-Bi/ZnO compared to ZnO and Bi/ZnO. BET surface area of AC-Bi/ZnO is higher than Bi/ZnO and ZnO. Higher surface area of the AC-Bi/ZnO enhances the photocatalytic activity. AC-Bi/ZnO has potential as use as a mediator for electrochemical analysis due to increases current and improves the relative electron transfer. AC-Bi/ZnO caused retarding the recombination reaction which occurs after excitation of semiconductor with UV light. Increase of the OH radicals formation during UV irradiation in AC-Bi/ZnO was observed due to the better separation of free carriers, however there was no linear relation of the photocatalyst ability to OH radicals formation on the content of AC and Bi in ZnO surfaces. AC-Bi/ZnO reveals enhanced photocatalytic activities as compared to ZnO and Bi/ZnO for the photodegradation and decolourization of MV under UV-light irradiation for 0 to 60 minutes. The mechanism of dye degradation is proposed for the higher photocatalytic activity of AC-Bi/ZnO.

Conflict of Interest

The authors declare no competing financial interest.

REFERENCES

1. S. Timur, I. C. Kantarli, S. Onenc and J. Yanik, *J. Anal. Appl. Pyrolysis* 2010, **89**, 129–136.

2. C. Namasivayam and D. Sangeetha, *J. Hazard. Mater. B,* 2006, **135**, 49–452.

3. F. K. Yuen and B. H. Hameed, J. Colloid Interface Sci., 2009, **149**, 19–27.

DOI: 10.1039/C4RA14463E

4. M. Hejazifar, S. Azizian, H. Sarikhani, Q. Li and D. Zhao, *J. Anal. Appl. Pyrolysis*, 2011, **92**, 258–266.

5. T. Robinson, G. McMillan, R. Marchant and P. Nigam, *Bioresource Technol.,* 2001, **77**, 247-255.

6. C. I. Pearce, J. R. Lloyd and J. T. Guthrie, *Dyes Pigm.,* 2003, **58**, 179-196.

7. A. M. Talarposhti, T. Donnelly and G. K. Anderson, *Water Res.,* 2001, **35**, 425-432.

8. H. C. Chu and K. M. Chen, *Process Biochem.,* 2002, **37**, 595–600.

9. Y. Fu and T. Viraraghavan, Adv. *Environ. Res.,* 2002, **7**, 239–247.

10. Z. Aksu, *Process Biochem.,* 2005, **40**, 997–1026.

11. A. Mittal, V. Gajbe and J. Mittal, *J. Hazard. Mater.,* 2008, **150**, 364–375.

12. R. Liu, P. Wang, X. Wang, H. Yu and J. Yu, *J. Phys. Chem. C*, 2012, **116**, 17721−17728.

13. K. T. Ranjit and I. Willner, *J. Phys. Chem. B,* 1998, **102**, 9397-9403.

14. S. Senthilvelan, V. L. Chandraboss, B. Karthikeyan, L. Natanapatham and M. Murugavelu, *Mater. Sci. Semicond. Process.,* 2013, **16**, 185-192.

15. V. L. Chandraboss, S. Senthilvelan, L. Natanapatham, M. Murugavelu, B. Loganathan and B. Karthikeyan, *J. Non-Cryst. Solids*., 2013, **368**, 23-28.

16. A. A. Khodja, T. Sehili, J. F. Pilichowski and P. Boule, *J. Photochem. Photobiol. A,* 2001, **141,** 231–239.

17. N. Daneshvar, D. Salari and A. R. Khataee, *J. Photochem. Photobiol. A,* 2004, **162**, 317–322.

18. H. Zhang, G. Chen and D. W. Bahnemann, *J. Mater. Chem*., 2009, **19**, 5089–5121.

19.K. Z. Zhang, B. Z. Lin, Y. L. Chen, B. H. Xu, X. T. Pian, J. D. Kuang and B. Li, *J. Colloid Interface Sci.,* 2011, **358**, 360–368.

View Article Online
DOI: 10.1039/C4RA14463E

20. S. Sakthivel, B. Neppolian, M. V. Shankar, B. Arabindoo, M. Palanichamy and V. Murugesan, *Sol. Energy Mater. Sol. Cells.,* 2003, **77**, 65–68.

21. C. A. K. Gouvea, F. Wypych, S. G. Moraes, N. Duran, N. Nagata and P. P. Zamora, *Chemosphere.*, 2000, **40**, 433–440.

22. C. Lizama, J. Freer, J. Baeza and H. D. Mansilla, *Catal. Today,* 2002, **76**, 235–246.

23. V.L. Chandraboss, B. Karthikeyan, J. Kamalakkannan, S. Prabha and S. Senthilvelan, *J. Nanopart.,* 2013, http://dx.doi.org/10.1155/2013/507161.

24. J. Yu, J. C. Yu, B. Cheng and X. Zhao, *J. Sol-Gel Sci. Technol*., 2002, **24**, 39–48.

25. S. Bagheri, K. G. Chandrappa and S. B. A. Hamid, *Der. Pharma. Chemica.,* 2013, **5**, 265–270.

26. F. Chekin, S. Bagheri and S. B. A. Hamid, *Anal. Methods,* 2012, **4**, 2423–2428.

27. J. H. Li, R. Y. Hong, M. Y. Li, H. Z. Li, Y. Zheng and J. Ding, *Prog. Org. Coat*., 2009, **64**, 504-509.

28. J. Yu and X. Yu, *Environ. Sci. technol.,* 2008, **42**, 4902–4907.

29. K.G. Chandrappa, T. V. Venkatesha, K. Vathsala and C. Shivakumara, *J. Nanopart. Res.,* 2010, **12** 2667–2678.

30. S. Suwanboon, P. Amornpitoksuk, A. Haidoux and J. C. Tedenac, *J. Alloys Compd*., 2008, **462**, 335–339.

31. V. L. Chandraboss, L. Natanapatham, B. Karthikeyan, J. Kamalakkannan, S. Prabah and S. Senthilvelan, *Mater. Res. Bull.,* 2013, **48**, 3707–3712.

32. A. P. A. Oliveira, J. F. Hochepied, F. Grillon, M. H. Berger, C*hem. Mater*. 2003, **15**, 3202–3207.

33 J. Zhang, F. Shi, J. Lin, D. Chen, J. Gao, Z. Huang, X. Ding and C. Tang, *Chem. Mater.* 2008, **20***,* 2937–2941.

34. L.Wang and M. Muhammed, *J. Mater. Chem*., 1999, **9**, 2871–2878.

View Article Online
DOI: 10.1039/C4RA14463E

35. J. Li, Y. Yu and L. Zhang, *Nanoscale,* 2014, **6**, 8473–8488.

36. T. Jia, W. Wang, F. Long, Z. Fu, H. Wang and Q. Zhang, *J. Alloys Compd.,* 2009, **484**, 410–415.

37. S. Senthilvelan, V. L. Chandraboss, B. Karthikeyan, M. Murugavelu, B. Loganathan and L. Natanapatham, *AIP Conf. Proc.,* 2012, **1461**, 395-398.

38. B. Donkova, D. Dimitrov, M. Kostadinov, E. Mitkova and D. Mehandjiev, *Mater. Chem. Phys.,* 2010, **123,** 563–568.

39. S. Gao, X. Jia, S. Yang, Z. Li and K. Jiang, *J. Solid State Chem.,* 2011, **184**, 764–769.

40. J. B. Zhong, J. Z. Li, Y. Lu, X. Y. He, J. Zeng, W. Hu and Y. C. Shen, *Appl. Surf. Sci.,* 2012, **258**, 4929– 4933.

41. H. G. Kim, D. W. Hwang and J. S. Lee, *J. Am. Chem. Soc.,* 2004, **126**, 8912–8913.

42. L. S. Zhang, H. L. Wang, Z. G. Chen, P. K. Wong and J. S. Liu, *Appl. Catal. B,* 2011, **106**, 1–13.

43. D. Li, Y. Zhang, Y. Zhang, X. Zhou and S. Guo, *J. Hazard. Mater.,* 2013, **258**, 42– 49.

44. J. Ru, Z. Huayue, L. Xiaodong and X. Ling, *Chem. Eng. J.*, 2009, **152**, 537-542.

45. N. Kannan and M. M. Sundaram, *Dyes Pigm.,* 2001, **51,** 25-40.

46. C. Namasivayam and D. Kavitha, *Dyes Pigm.,* 2002, **54**, 47-58.

47. P. K. Malik, *Dyes Pigm.,* 2003, **56,** 239-249.

48. G. Mezohegyi, P. Frank, V. D. Zee, J. Font, A. Fortuny and A. Fabregat, *J. Environ. Manage.,* 2012, **102**, 148-164.

49. J. Arana, J. M. Dona-Rodrıguez, E. Tello Rendón, C. Garriga i Cabo, O. Gonzalez-D´ıaz, J. A. Herrera-Melian, J. Perez-Pena, G. Colon and J. A. Navıo, *Appl.Catal., B,* 2003, **44**, 153–160.

50. N. Sobana, B. Krishnakumar and M. Swaminathan, *Mater. Sci. Semicond. Process.*, 2013, **16**, 1046–1051.

View Article Online
DOI: 10.1039/C4RA14463E

51. K. I. Ishibashi, A. Fujishima, T. Watanabe and K. Hashimoto, *Electrochem. Commun*., 2000, **2** 207–210.

52. J. Zhang, Y. Wu, M. Xing, S. A. K. Leghari and S. Sajjad, *Energy Environ. Sci*., 2010, **3**, 715–726.

53. B. Krishnakumar, B. Subash and M. Swaminathan, *Sep. Purif. Technol*., 2012, **85**, 35−44.

54. D. Yiamsawas, K. Boonpavanitchakul and W. Kangwansupamonkon, *J. Microsc. Soc. Thailan.*, 2009, **23**, 75−78.

55. J. Zhang, S. Liu, J. Yu and M. Jaroniec, *J. Mater. Chem*., 2011, **21**, 14655–14662.

56. C. Chen, B. Yu, J. Liu, Q. Dai and Y. Zhu, *Mater. Lett.,* 2007, **61**, 2961-2964.

57. Y. P. Du, Y. W. Zhang, L. D. Sun and C. H. Yan, *J. Phys. Chem. C,* 2008, **112**, 12234–12241.

58. B. Subash, B. Krishnakumar, M. Swaminathan and M. Shanthi, *Langmuir,* 2013, **29**, 939−949.

59. S. Balachandran and M. Swaminathan, *Dalton Trans*., 2013, **42**, 5338–5347.

60. S. C. Lyu, Y. Zhang, H. Ruh, H. Lee, H. Shim, E. Suh and C. J. Lee, *Chem. Phys. Lett*., 2002, **363**, 134-138.

61. L. Bergman, X. B. Chen, J. L. Morrison, J. Huso and A. P. Purdy, *J. Appl. Phys.,* 2004, **96**, 675-682.

62. J. Wang and L. Gao, *Solid State Commun*., 2004, **132**, 269-271.

63. B. Subash, B. Krishnakumar, B. Sreedhar, M. Swaminathan and M. Shanthi, *Superlattices Microstruct*., 2013, **54**, 155–171.

64. C. Karunakaran, S. SakthiRaadha, P. Gomathisankar and P. Vinayagamoorthy, *Dalton. Trans*., 2013, **42**, 13855-13865.

65. B. Loganathan, V. L. Chandraboss, M. Murugavelu, S. Senthilvelan and B. Karthikeyan, *J. Sol-Gel Sci. Technol*., DOI 10.1007/s10971-014-3564-5.

View Article Online
DOI: 10.1039/C4RA14463E

66. J. F. Moudler, W. F. Stickle, P. E. Sobol and K. D. Bomben, Handbook of X-ray Photoelectron Spectroscopy, Perkin-Elmer, Eden Prairie, MN, 1992.

67. H. Ma, J. Han, Y. Fu, Y. Song, C. Yu and X. Dong, *Appl. Catal. B*, 2011, **102**, 417–423.

68. C. D. Wagner, W. M. Riggs, L. E. Davis and J. F. Moulder, Handbook of X-ray Photoelectron Spectroscopy, Perkin Elmer, Eden Prairie, 1979, p. 81.

69. Y. Schuhl, H. Baussart, R. Delobel, M. Le Bras, J. Leroy, L. G. Gengembre and J. Rimblot, *J. Chem. Soc., Faraday Trans. 1,* 1983, **79**, 2055.

70. X. Jing-jing, C. Min-dong and F. De-gang, *Trans. Nonferrous Met. Soc. China*, 2011, **21**, 340−345.

71. J. G. Yu, L. J. Zhang, B. Cheng and Y. R. Su, *J. Phys. Chem. C*, 2007, **111,** 10582-10589.

72. T. Sreethawong, Y. Yamadab, T. Kobayashi and S. Yoshikawa, *J. Mol. Catal. A*, 2005, **241**, 23-32.

73. S. Sajjad, S. A. K. Leghari and J. Zhang, *RSC Adv*., 2013, **3**, 1363-1367.

74. M. Zidan, W. T. Tan, Z. Zainal, A. H. Abdullah and J. K. Goh, *Int. J. Electrochem. Sci.*, 2010, **5**, 501-508.

75. M. M. Radhi, W. T. Tan, M. Z. B. A. Rahman and A. B. Kassim, *Res. J. Appl. Sci.*, 2010, **5**, 59-64.

76. Y. Zhao, C. Z. Li, X. H. Liu, F. Gu, H. B. Jiang, W. Shao, L. Zhang, and Y. He, *Mater. Lett.* 2007, **61**, 79-83.

77. P. M. Kumar, S. Badrinarayanan and M. Sastry, *Thin Solid Films,* 2000, **358**, 122-130.

78. L. J. Tomar and B.S. Chakrabarty, *Adv. Mat. Lett*. 2013, **4**, 64-67.

79. W. Xie, Y. Li, W. Sun, J. Huang, H. Xie and X. Zhao, *J. Photochem. Photobiol. A*, 2010, **216,** 149–155.

80. S. Zhang, J. Li, M. Zeng, J. Li, J. Xu and X. Wang, *Chem. Eur. J.* 2014, **20**, 9805–9812.

81. D. F. Li, Y. H. Guo, C. W. Hu, C. J. Jiang and E. B. Wang, *J. Mol. Catal. A*, 2004, **207,** 183-193.

View Article Online
DOI: 10.1039/C4RA14463E

82. K. Sahel, N. Perol, H. Chermette, C. Bordes, Z. Derriche and C. Guillard, *Appl. Catal. B,* 2007, **77**, 100-109.

83. T. Yu, X. Tan, L. Zhao, Y. X. Yin, P. Chen and J. Wei, *Chem. Eng. J.*, 2010, **157**, 86-92.

84. H. Fan, T. Jiang, L. Wang, D. Wang, H. Li, P. Wang, D. He and T. Xie, *J. Phys. Chem. C,* 2012, **116,** 2425-2430.

85. S. Zhang, J. Li, M. Zeng, G. Zhao, J. Xu, W. Hu and X. Wang, *Appl. Mater. Interfaces,* 2013, **5**, 12735−12743.

86. L. Wu, J. C. Yu and X. Y. Fu, *J. Mol. Catal. A,* 2006, **244**, 25–32.

87. S. Balachandran and M. Swaminathan, *J. Phys. Chem. C*, 2012, **116**, 26306-26312.

View Article Online
DOI: 10.1039/C4RA14463E

Captions for Scheme, Figures and Table

Scheme 1. Schematic representation for the synthesis of AC-Bi/ZnO nanocomposite material.

Fig. 1. Dye effluents onto the AC-Bi/ZnO surface is desirable for photodegradation kinetics.

Fig. 2. HR-SEM images of (a) Bi/ZnO, (b) AC-Bi/ZnO nanocomposite material, EDX analysis of (c) Bi/ZnO, (d) AC-Bi/ZnO nanocomposite material.

Fig. 3. XRD patterns of (a) ZnO nanomaterial, (b) Bi/ZnO nanocomposite material and (c) AC-Bi/ZnO nanocomposite material.

Fig. 4. FT-RAMAN spectra of (a) ZnO nanomaterial, (b) Bi/ZnO nanocomposite material and (c) AC-Bi/ZnO nanocomposite material.

Fig. 5. PL spectra of (a) ZnO nanomaterial, (b) Bi/ZnO nanocomposite material and (c) AC-Bi/ZnO nanocomposite material

Fig. 6. Direct band gap of (a) AC-Bi/ZnO, (b) Bi/ZnO, (c) ZnO and (d) Plot of Kubelka–Munk function versus energy of the light absorbed of the catalysts

Fig. 7. XPS survey spectrum of AC-Bi/ZnO nanocomposite material

Fig. 8. N_2 adsorption–desorption isotherms of (a) ZnO (b) Bi/ZnO and (c) AC-Bi/ZnO (Inset: BJH desorption pore distribution)

Fig. 9. CVs of (a) uncoated GCE with 0.1 M KCl (green curve), (b) ZnO coated GCE in 0.1 M KCl (blue curve) and (c) AC-Bi/ZnO coated GCE in 0.1 M KCl (red curve).

Fig. 10. PL spectra of AC-Bi/ZnO under excitation at 330 nm in coumarin solution (a) UV-light irradiation of AC-Bi/ZnO at 60 min and (b) UV-light irradiation of AC-Bi/ZnO obtained using different time intervals (0, 30 and 60 mins).

View Article Online
DOI: 10.1039/C4RA14463E

Fig. 11. Absorption spectra changes of methyl violet solution (2×10^{-4} M, 40 mL) in the presence of photocatalysts (a) ZnO, (b) Bi/ZnO and (c) AC-Bi/ZnO under UV-light (365 nm) irradiation at 10 minute interval. (d) Comparative studies of photocatalytic activity (absorbance vs time (min)) of ZnO, Bi/ZnO and AC-Bi/ZnO photocatalysts for photodegradation and decolourization of MV under UV-light (365 nm) irradiation at 10 minute interval.

Fig. 12. (a) Comparison of photocatalytic activity (dye decolouration (%) vs time (min)) of decolouration of MV dye by ZnO, Bi/ZnO and AC-Bi/ZnO under UV-light (365 nm) irradiation at 10 minute interval. (b) Comparisons of photocatalytic activity (Concentration (M) vs time (min)) of decolouration of MV dye by ZnO, Bi/ZnO and AC-Bi/ZnO under UV-light (365 nm) irradiation at 10 minute interval.

Fig. 13. (a) Kinetic of methyl violet degradation upon irradiation and (b) Photodegraded efficiencies for the ZnO, Bi/ZnO and AC-Bi/ZnO, variations in $\ln(C_0/C)$ as function of irradiation time and linear fits of catalysts.

Fig. 14. Schematic illustration of AC supported Bi-doped ZnO mechanism for photocatalytic process.

Table. 1. Surface properties of the materials

View Article Online
DOI: 10.1039/C4RA14463E

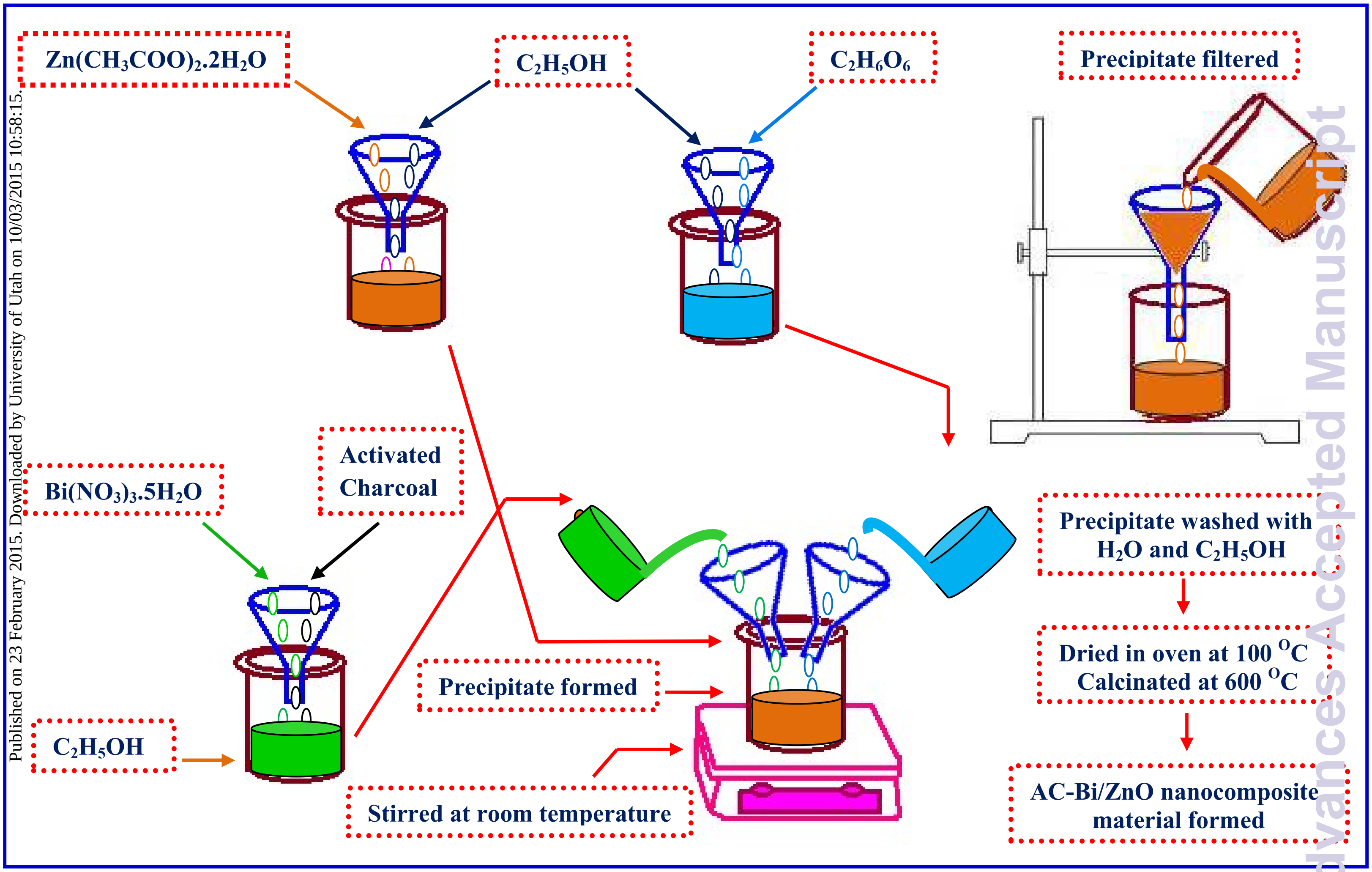

Scheme 1. Schematic representation for the synthesis of AC-Bi/ZnO nanocomposite material

View Article Online
DOI: 10.1039/C4RA14463E

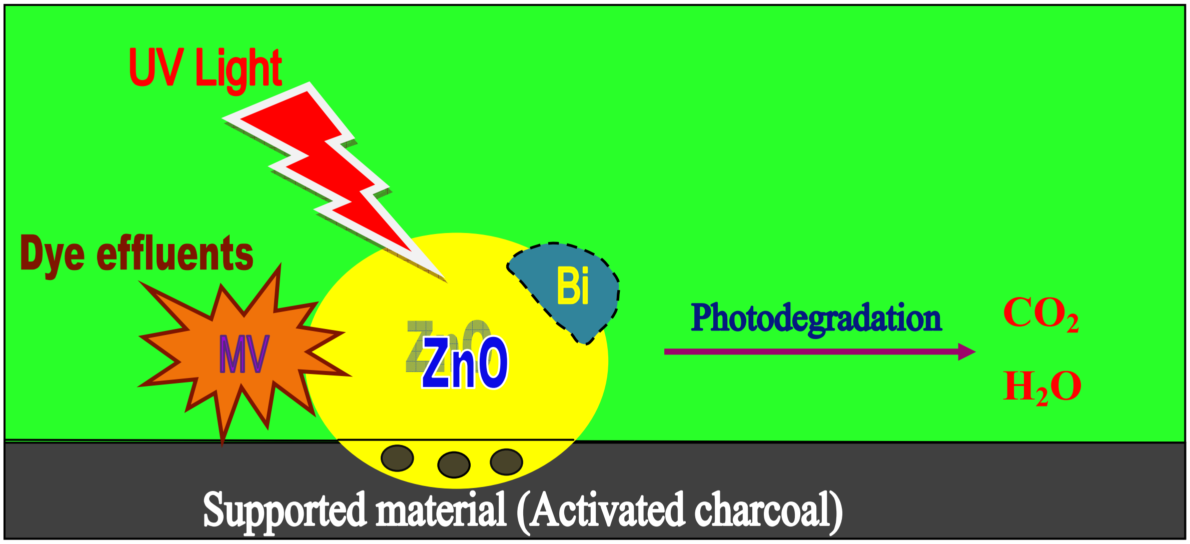

Fig. 1. Dye effluents onto the AC-Bi/ZnO surface is desirable for photodegradation kinetics

View Article Online
DOI: 10.1039/C4RA14463E

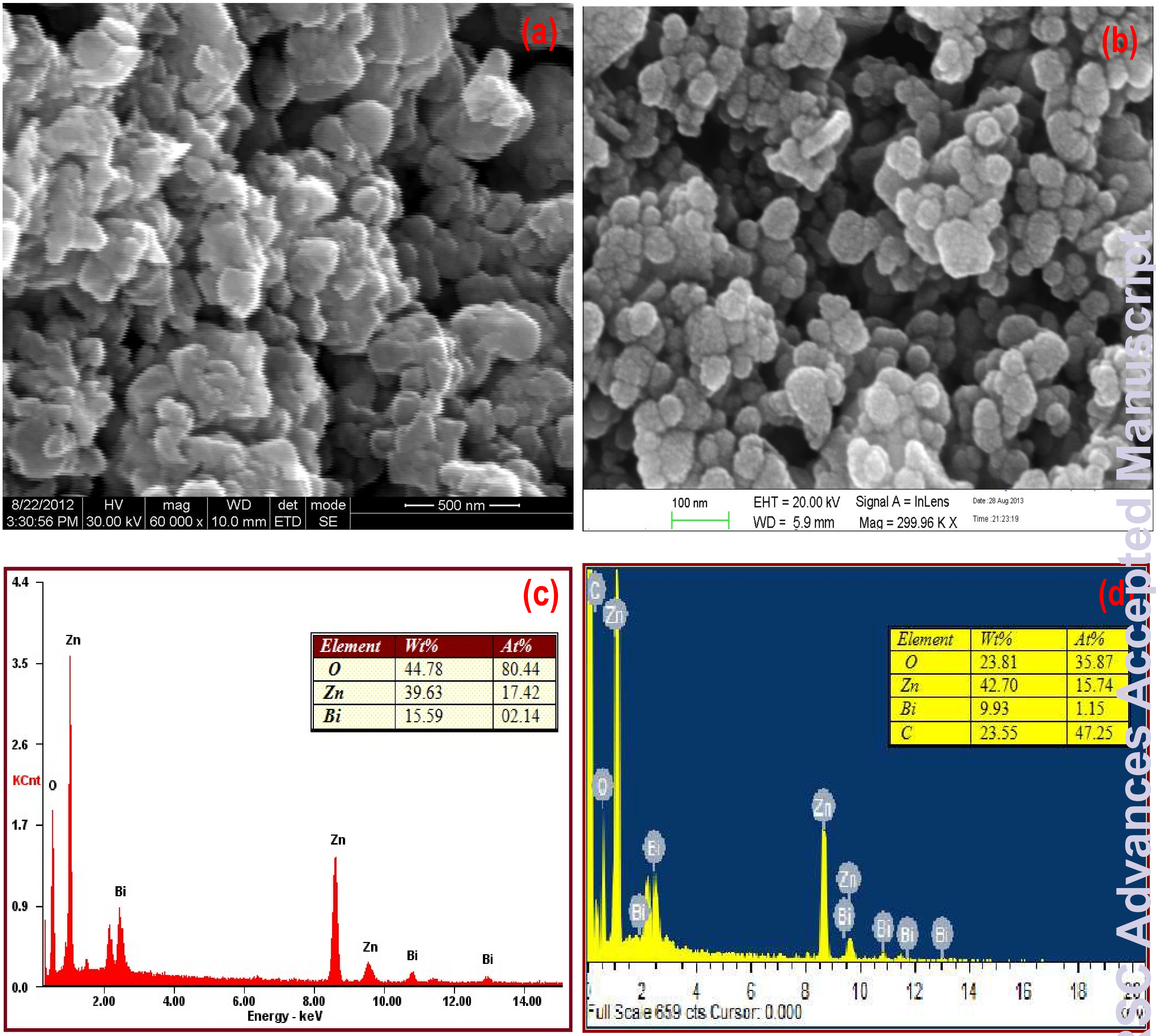

Element	Wt%	At%
O	44.78	80.44
Zn	39.63	17.42
Bi	15.59	02.14

Element	Wt%	At%
O	23.81	35.87
Zn	42.70	15.74
Bi	9.93	1.15
C	23.55	47.25

Fig. 2. HR-SEM images of (a) Bi/ZnO, (b) AC-Bi/ZnO nanocomposite material, EDX analysis of (c) Bi/ZnO and (d) AC-Bi/ZnO nanocomposite material

View Article Online
DOI: 10.1039/C4RA14463E

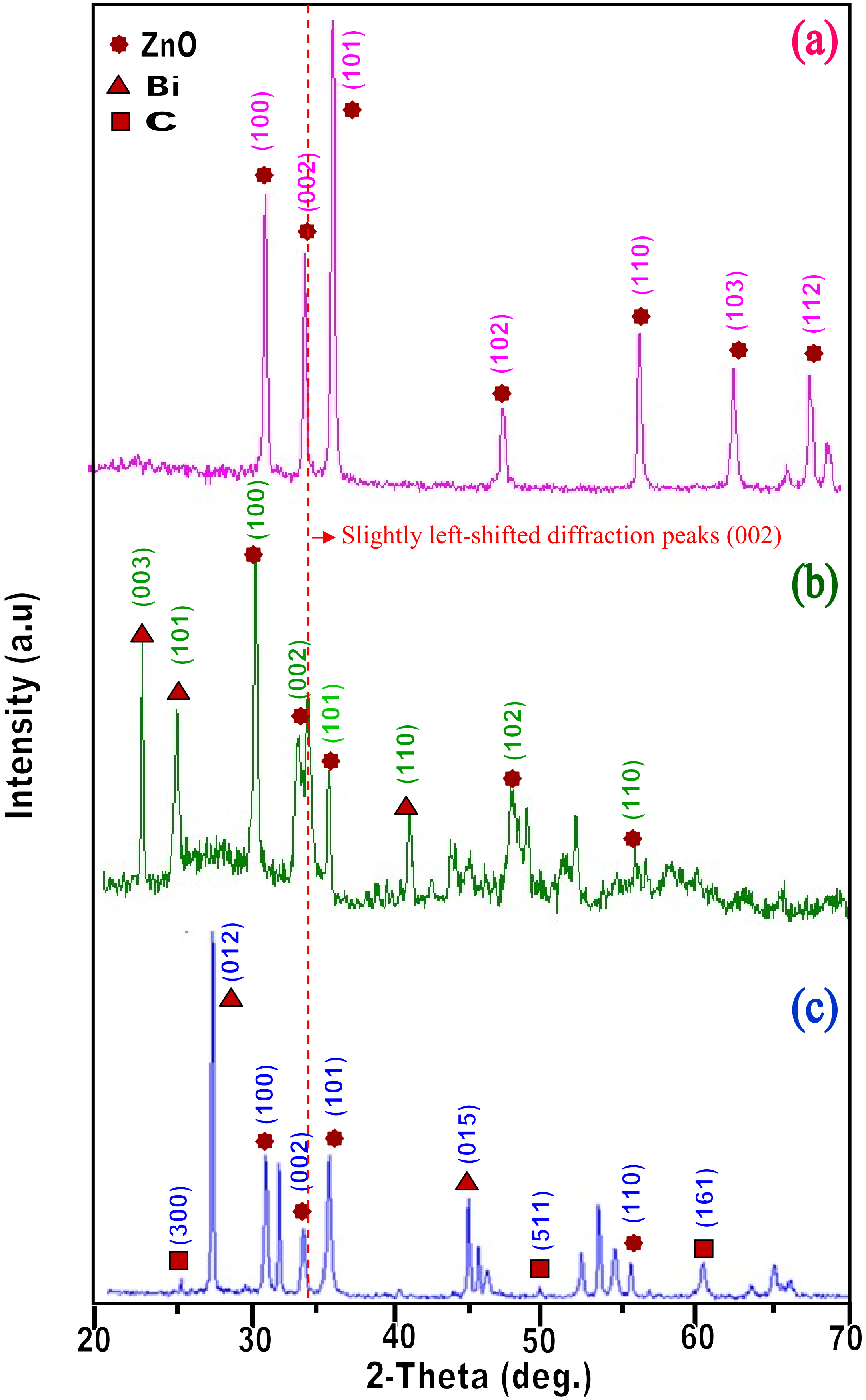

Fig. 3. XRD patterns of (a) ZnO nanomaterial, (b) Bi/ZnO nanocomposite material and (C) AC-Bi/ZnO nanocomposite material

View Article Online
DOI: 10.1039/C4RA14463E

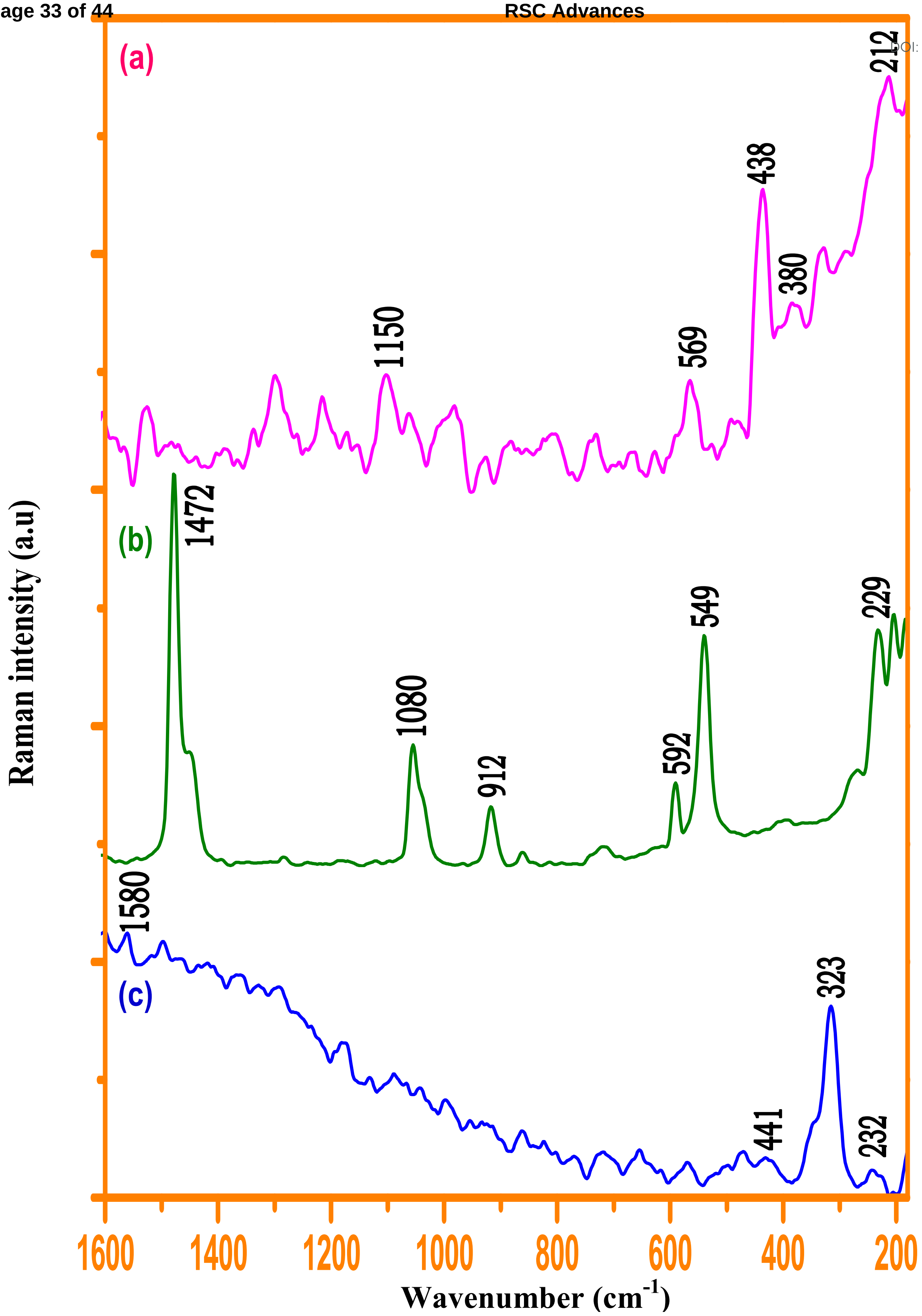

Fig. 4. FT-RAMAN spectra of (a) ZnO nanomaterial, (b) Bi/ZnO nanocomposite material and (c) AC-Bi/ZnO nanocomposite material

View Article Online
DOI: 10.1039/C4RA14463E

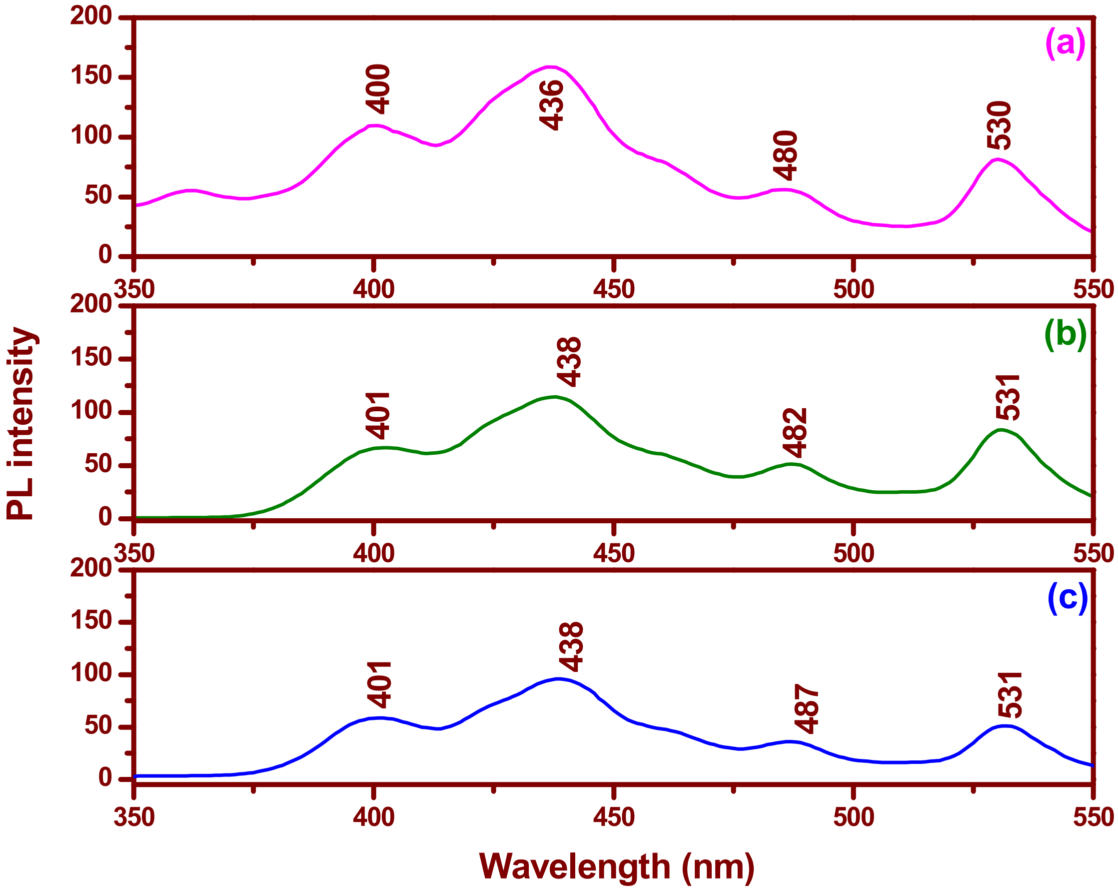

Fig. 5. PL spectra of (a) ZnO nanomaterial, (b) Bi/ZnO nanocomposite material and (c) AC-Bi/ZnO nanocomposite material

View Article Online
DOI: 10.1039/C4RA14463E

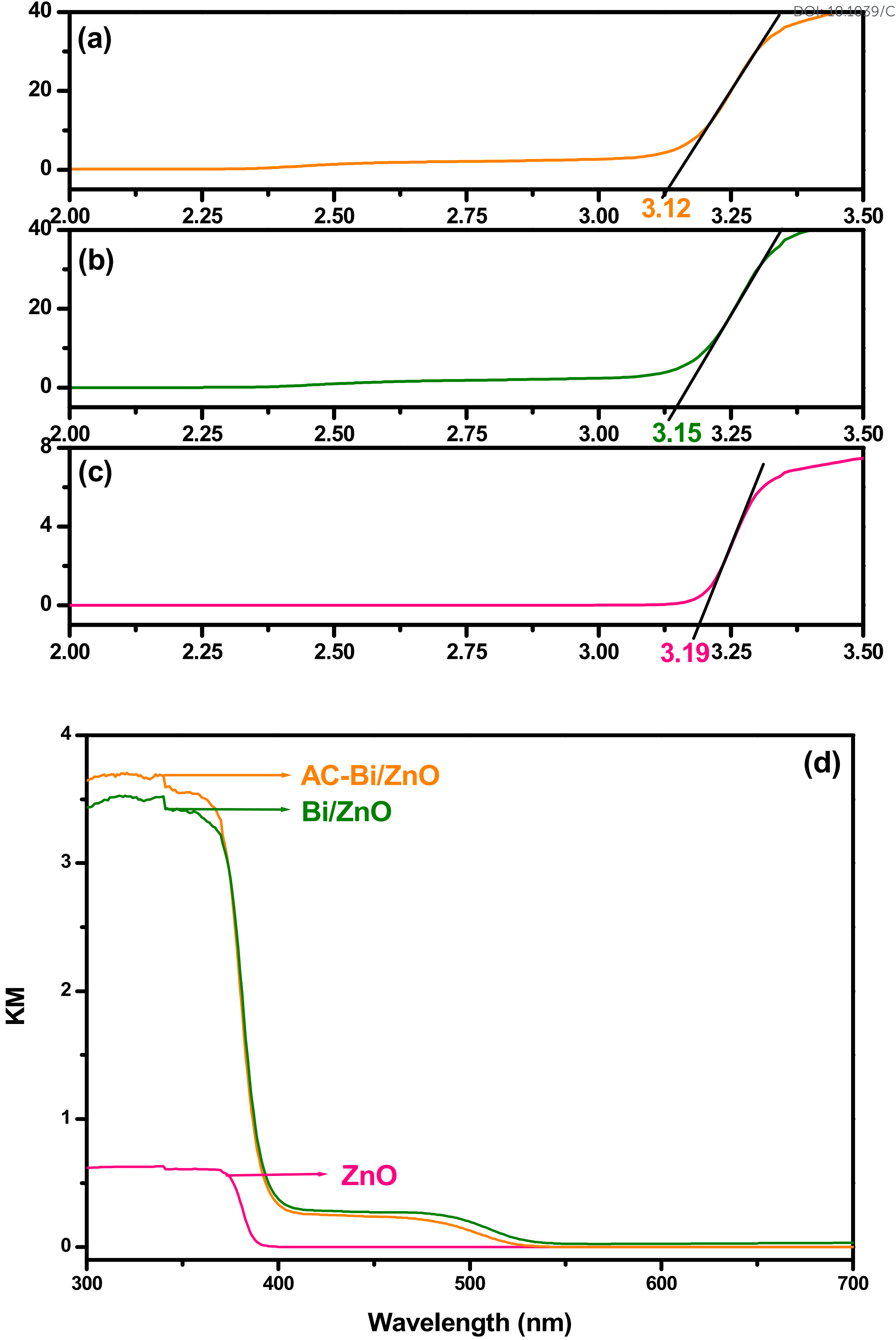

Fig. 6. Direct band gap of (a) AC-Bi/ZnO, (b) Bi/ZnO, (c) ZnO and (d) Plot of Kubelka–Munk function versus energy of the light absorbed of the catalysts

View Article Online
DOI: 10.1039/C4RA14463E

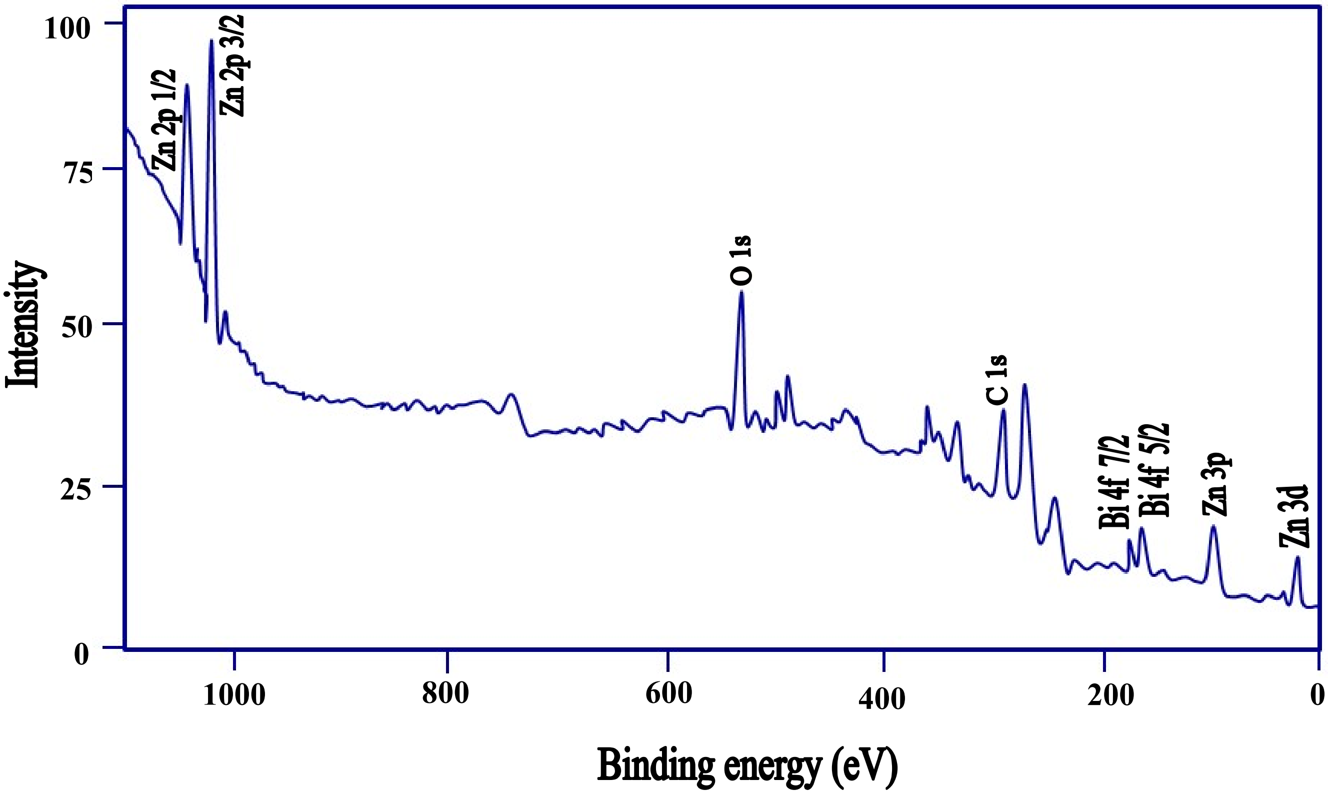

Fig. 7. XPS survey spectrum of AC-Bi/ZnO nanocomposite material

View Article Online
DOI: 10.1039/C4RA14463E

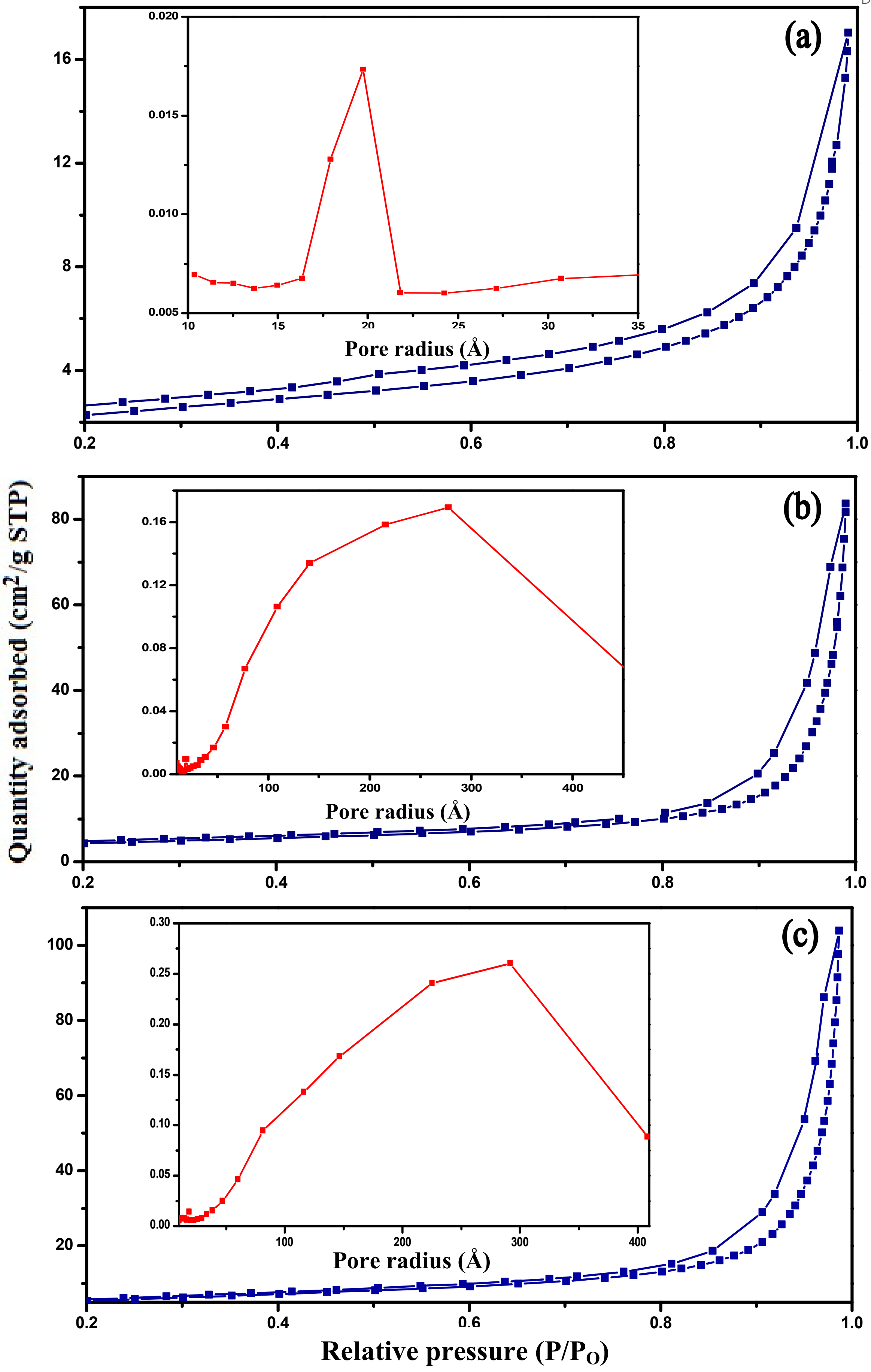

Fig. 8. N_2 adsorption–desorption isotherms of (a) ZnO (b) Bi/ZnO and (c) AC-Bi/ZnO (Inset: BJH desorption pore distribution)

View Article Online
DOI: 10.1039/C4RA14463E

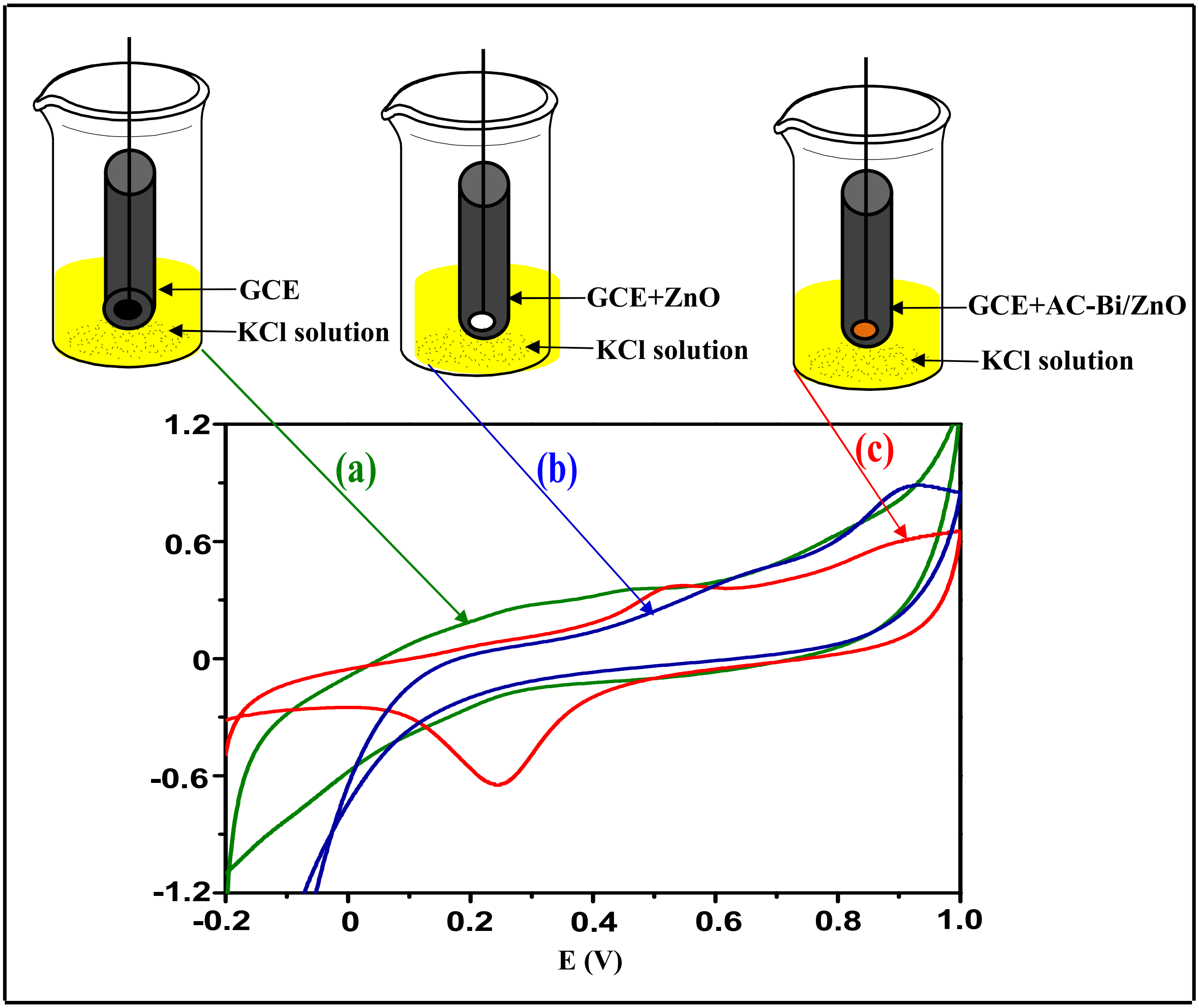

Fig. 9. CVs of (a) uncoated GCE with 0.1 M KCl (green curve), (b) ZnO coated GCE in 0.1 M KCl (blue curve) and (c) AC-Bi/ZnO coated GCE in 0.1 M KCl (red curve).

View Article Online
DOI: 10.1039/C4RA14463E

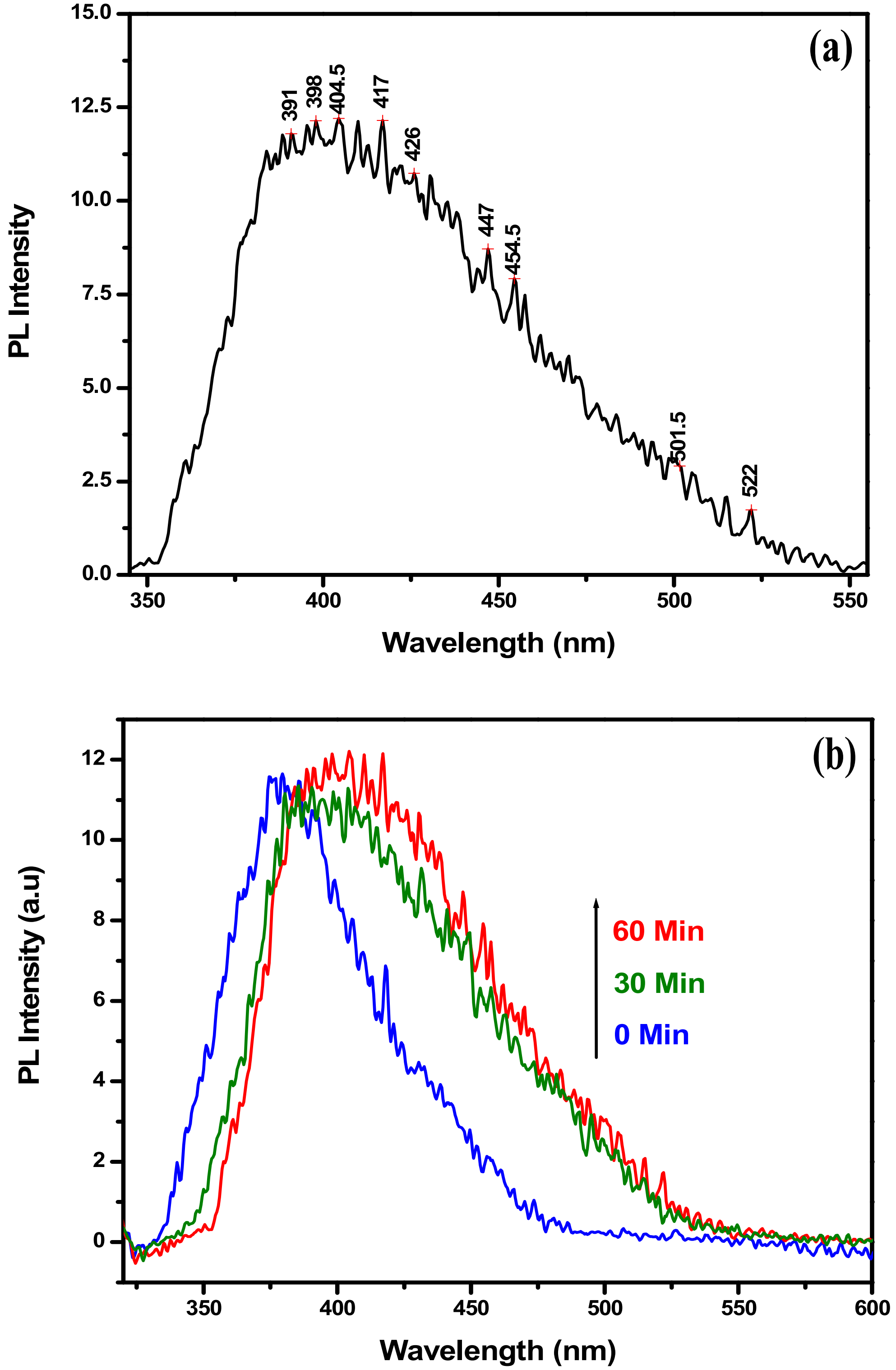

Fig. 10. PL spectra of AC-Bi/ZnO under excitation at 330 nm in coumarin solution (a) UV-light irradiation of AC-Bi/ZnO at 60 min and (b) UV-light irradiation of AC-Bi/ZnO obtained using different time intervals (0, 30 and 60 mins).

View Article Online
DOI: 10.1039/C4RA14463E

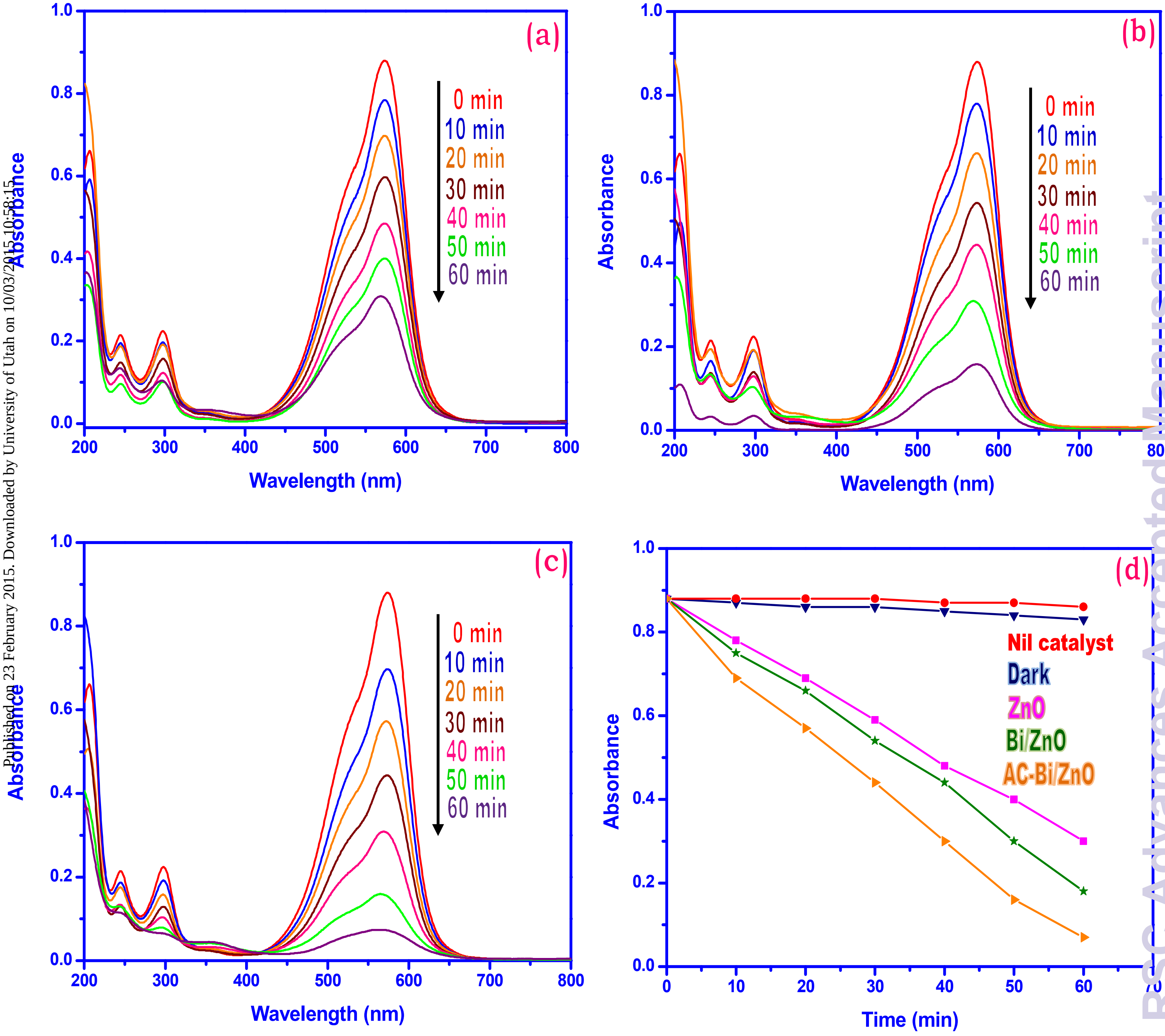

Fig. 11. Absorption spectra changes of methyl violet solution (2×10^{-4} M, 40 mL) in the presence of photocatalysts (a) ZnO, (b) Bi/ZnO and (c) AC-Bi/ZnO under UV-light (365 nm) irradiation at 10 minute interval. (d) Comparative studies of photocatalytic activity (absorbance vs time (min)) of ZnO, Bi/ZnO and AC-Bi/ZnO photocatalysts for photodegradation and decolourization of MV under UV-light (365 nm) irradiation at 10 minute interval.

View Article Online
DOI: 10.1039/C4RA14463E

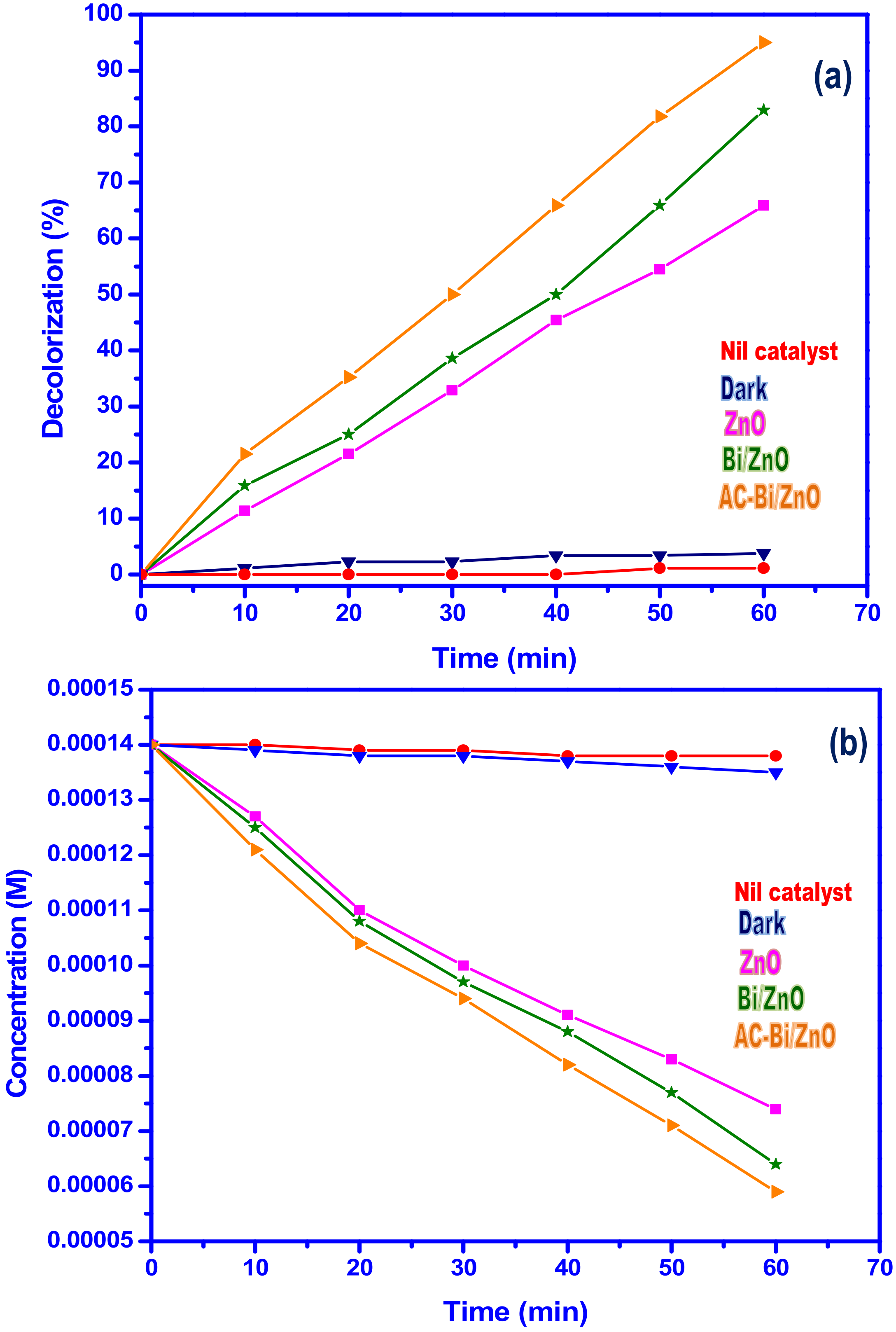

Fig. 12. (a) Comparison of photocatalytic activity (dye decolouration (%) vs time (min)) of ZnO, Bi/ZnO and AC-Bi/ZnO under UV-light (365 nm) irradiation at 10 minute interval. (b) Comparison of photocatalytic activity (Concentration (M) vs time (min)) of ZnO, Bi/ZnO and AC-Bi/ZnO under UV-light (365 nm) irradiation at 10 minute interval.

View Article Online
DOI: 10.1039/C4RA14463E

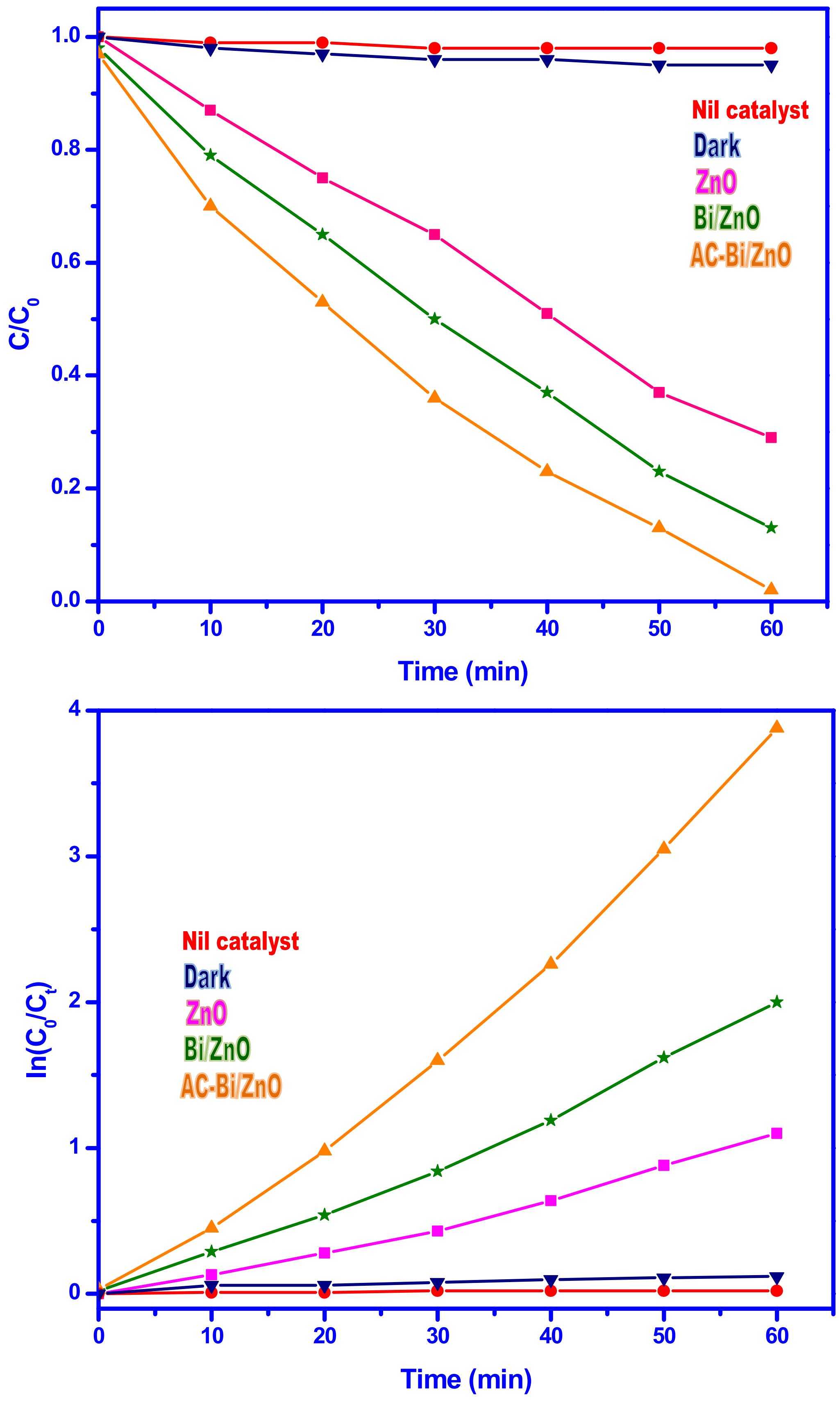

Fig. 13. (a) Kinetic of methyl violet degradation upon irradiation and (b) Photodegraded efficiencies for the ZnO, Bi/ZnO and AC-Bi/ZnO, variations in ln(C_0/C) as function of irradiation time and linear fits of catalysts.

View Article Online
DOI: 10.1039/C4RA14463E

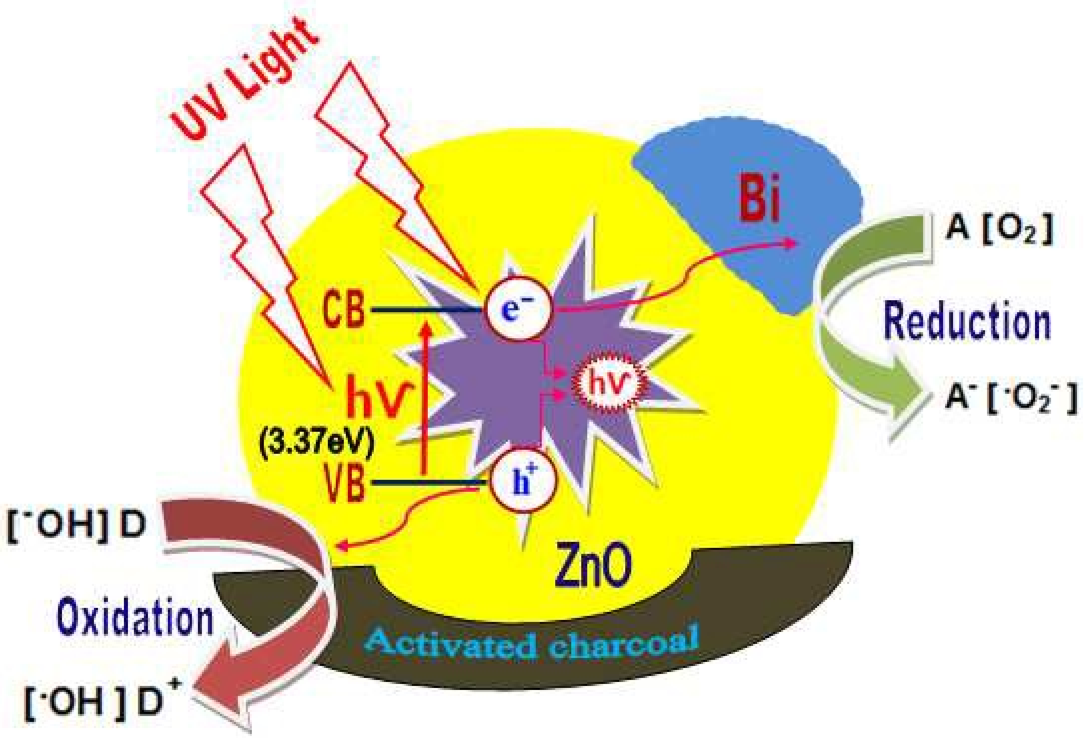

Fig. 14. Schematic illustration of AC supported Bi-doped ZnO mechanism for photocatalytic process

View Article Online
DOI: 10.1039/C4RA14463E

Table. 1. Surface properties of the materials

Properties	ZnO	Bi/ZnO	AC-Bi/ZnO
BET surface area	8.3 m^2/g^{-1}	15.3 m^2/g^{-1}	19.4 m^2/g^{-1}
Total pore volume (single point)	0.026 cm^3/g^{-1}	0.12 cm^3/g^{-1}	0.16 cm^3/g^{-1}